Bulletin of the Seismological Society of America, Vol. 102, No. 3, pp. 999–1017, June 2012, doi: 10.1785/0120110182

Nonlinear Dimensional Analysis of Trapezoidal Valleys Subjected to Vertically Propagating *SV* Waves

by F. Gelagoti, R. Kourkoulis, I. Anastasopoulos, and G. Gazetas

Abstract This paper studies the seismic response of soil basins emphasizing the sensitivity of 2D dynamic response to geometric and material properties. This is accomplished through a formal dimensional analysis accounting for fully inelastic soil response thus augmenting the generalization potential of the results, and providing a novel framework for future research on the subject. It is shown that 2D valley response may be described through the following key dimensionless parameters: (1) the valley shape factor s, expressing the slope inclination; (2) the impedance ratio i, which expresses the stiffness of the soil relative to the bedrock; (3) the wavelength ratio λ_S, which is a function of soil stiffness and seismic excitation frequency; (4) the rigidity ratio v, expressing the stiffness of the soil relative to its strength; and (5) the resistance ratio r, which expresses the degree of soil nonlinearity. The effectiveness of the dimensional formulation is verified through the numerical analysis of equivalent valleys, assuming elastic and nonlinear soil response. Finally, a parametric study is conducted to gain insight on the effects of the introduced dimensionless parameters on the dynamic response of trapezoidal alleys. It is shown that decreasing the valley slope or the wavelength ratio promotes wave reflections within the wedge, thus enhancing the possibility of wave interferences and subsequently leading to 2D aggravation on the valley surface. On the other hand, the geometry-dependent parasitic vertical acceleration increases as the valley slope becomes steeper. As the degree of soil nonlinearity increases, 2D phenomena tend to become localized close to the valley edges.

Introduction

It is well known that local geologic conditions, particularly as materialized within alluvial basins, may strongly influence the nature and intensity of ground shaking. Hence, conventional 1D modeling would generally fail to reproduce the complex wave scattering phenomena introduced by the nonlevel geometry of a sedimentary deposit. Such phenomena include: (1) generation of surface waves at the lateral boundaries, which tend to increase both the amplitude and the duration of ground motion; (2) amplification and resonance induced by low-velocity surface layers; and (3) multiple refractions of incoming rays due to the 2D or 3D geometry of the alluvial basin, which are responsible not only for aggravating the response but also for producing a quite destructive parasitic vertical component (e.g., Gelagoti *et al.*, 2010).

Earthquake events over the last 40 years have offered an extensive list of documented occurrences of wave scattering effects on the modification of surface ground motion. Some early examples include the response of the Caracas Valley during the 1967 earthquake (Papageorgiou and Kim, 1991) or the highly nonuniform damage distribution pattern in Kirovakan after the Spitak earthquake in Armenia (Borcherdt *et al.*, 1989; Yegian *et al.*, 1994). The role of surface waves in the 1971 San Fernando earthquake that stroke the deep California basin was initially revealed through measurements (Hanks, 1975) and later confirmed by Vidale and Helmberger (1988). Localized heterogeneities of surface soft clay layers were also accountable for the completely diverse motion recorded at two adjacent sites during the 1985 Michoacan earthquake (Bard *et al.*, 1988; Chávez-García and Bard, 1989). Local site conditions were proven to play a quite prevailing role in the damage distribution pattern of the devastating Northridge (1994) and Kobe (1995) earthquakes (Kawase, 1996; Pitarka *et al.*, 1998; Scrivner and Helmberger, 1999), while most recently, recordings from the latest strong earthquakes (2010–2011) in Christchurch, New Zealand, have clearly indicated strong ground-motion amplification phenomena attributable to valley effects (Cubrinovski and Green, 2010).

Motivated by the impact of such events, substantial research effort has been devoted aiming to advance the understanding on wave propagation characteristics in alluvial valleys. Pioneering work in this area commenced in the early 1960s, mainly dealing with the study of elastic

wave propagation in horizontally stratified media with irregular interfaces (Herrera, 1964; Tsai 1969; Aki and Larner, 1970; Boore, 1970). Closed form rigorous analytical solutions on 2D wave diffraction were obtained by Trifunac (1971, 1973) and Wong and Trifunac (1974) for valleys and canyons of rather simple geometries subjected to plane *SH* waves. The realm of recently advanced powerful numerical algorithms (such as boundary elements, finite differences, and finite and spectral elements) has further enhanced the research potential on the subject, providing the means to delineate the key factors controlling site response during a seismic event (Sánchez-Sesma *et al.*, 1993; Fishman and Ahmad, 1995; Sánchez-Sesma and Luzon, 1995; Bard and Bouchon, 1980a, b; Harmsen and Harding, 1981; Hill *et al.*, 1990; Pitarka and Irikura, 1996; Zhang and Papageorgiou, 1996; Bielak and Ghattas, 1999; Olsen *et al.*, 2006; Archuleta *et al.*, 2003; Hartzell *et al.*, 2003). Besides 1D soil stratigraphy and basin geometry, it has been shown that the strong ground motion may be dramatically affected by the source characteristics (i.e., the type and angle of incidence of incoming waves), the specific features of the velocity structure (i.e., the geometry of lateral heterogeneities, the impedance contrast of subsequent layers, etc.), and the degree of mobilized soil nonlinearity.

Apparently, the significant amount of uncertainties associated with the dynamic response of alluvial valleys will unavoidably produce results which are exceptionally sensitive to the individual characteristics of the problem under study. This paper initially utilizes a specific example to underscore the sensitivity of valley response on soil stiffness. This is pursued by a formal dimensional analysis accounting for fully inelastic soil response. Such an approach enables the production of dimensionless results, thus aiming to set a framework of conclusions of generalized (rather than case-specific) applicability. To this end, this paper examines the response of trapezoidal valleys of various symmetrical shapes and certain material characteristics (all inspired by well-known existing formations) excited by vertically propagating plane *SV* waves.

Analysis Methodology

As shown in Figure 1a, an idealized trapezoidal alluvial valley of width $2L$ and depth d is analyzed in 2D, assuming plane strain conditions. The problem is analyzed in the time domain employing the finite element (FE) method. The valley models have been excited by Ricker-type pulse excitations of varying characteristic frequencies f_o. Two indicative examples, a higher frequency Ricker-3 and a lower frequency Ricker-1 pulse are presented in Figure 1b. Very finely discretized quadrilateral continuum elements have been used in soil modeling so as to ensure realistic representation of the propagating wavelengths. The element size has been chosen so that at least 10 elements correspond to the smallest expected wavelength (given that in nonlinear problems the wavelength is expected to reduce with the increasing degree of plastification). Radiation damping is taken into account by introducing appropriate absorbing boundaries at the base of the numerical model. Free-field boundaries responding as shear beams are placed at the two lateral boundaries of the model to simulate the motion produced by in-plane vertically incident *SV* waves.

The numerical analysis methodology employed herein has been extensively validated against a recorded seismic response in Gazetas *et al.* (1993) and Gelagoti *et al.* (2010). Rayleigh damping is introduced to effectively reproduce visco–elastic soil response, while nonlinear hysteretic soil behavior is modeled by employing a kinematic hardening constitutive model, incorporating the Von Mises failure criterion and an associative plastic flow rule. The model has been validated against centrifuge experiments and shown to effectively capture the undrained cyclic soil response (Anastasopoulos *et al.*, 2011).

The evolution law of the model consists of two components: a nonlinear kinematic hardening component, which describes the translation of the yield surface in the stress space (defined through the backstress parameter α), and an isotropic hardening component, which defines the size of the yield surface σ_o as a function of plastic deformation. Calculation of the model parameters requires the knowledge of (a) soil strength S_u, (b) small-strain stiffness G_o or V_{so}, and (c) stiffness reduction G-γ and ξ-γ curves to calibrate parameter λ. Figure 2a compares the calibrated numerical model prediction in terms of G-γ and ξ-γ curves against the published data of Ishibashi and Zhang (1993), while Figure 2b plots the numerical shear strain versus shear stress loops produced when subjecting a soil element to cyclic shear deformation of gradually increasing amplitude. The model has been successfully adopted in the analysis of the seismic behavior of an alluvial basin by Gelagoti *et al.* (2010).

The Necessity for Dimensional Analysis

2D valley effects have been proven to be a function of a number of parameters such as the shape and dimensions of the valley, the soil properties, and the characteristics of the seismic excitation. Consequently, a complete parametric investigation would be a formidable task, and the study of specific cases, despite offering valuable insights on the governing mechanisms affecting the response, cannot lead to results and conclusions of more general applicability. Such shortcomings may be substantially overcome through dimensional analysis.

To persuasively underscore the limited generality of conclusions based on specific case studies, it is herein attempted to demonstrate the sensitivity of valley response to two key problem parameters: soil stiffness, expressed through the shear wave velocity V_S of the alluvium (assuming elastic soil response); and soil nonlinearity (using the aforementioned constitutive model). The specific numerical example adopted refers to a relatively mild trapezoidal valley of depth $d = 24$ m (Fig. 1), inspired by the geometry of the

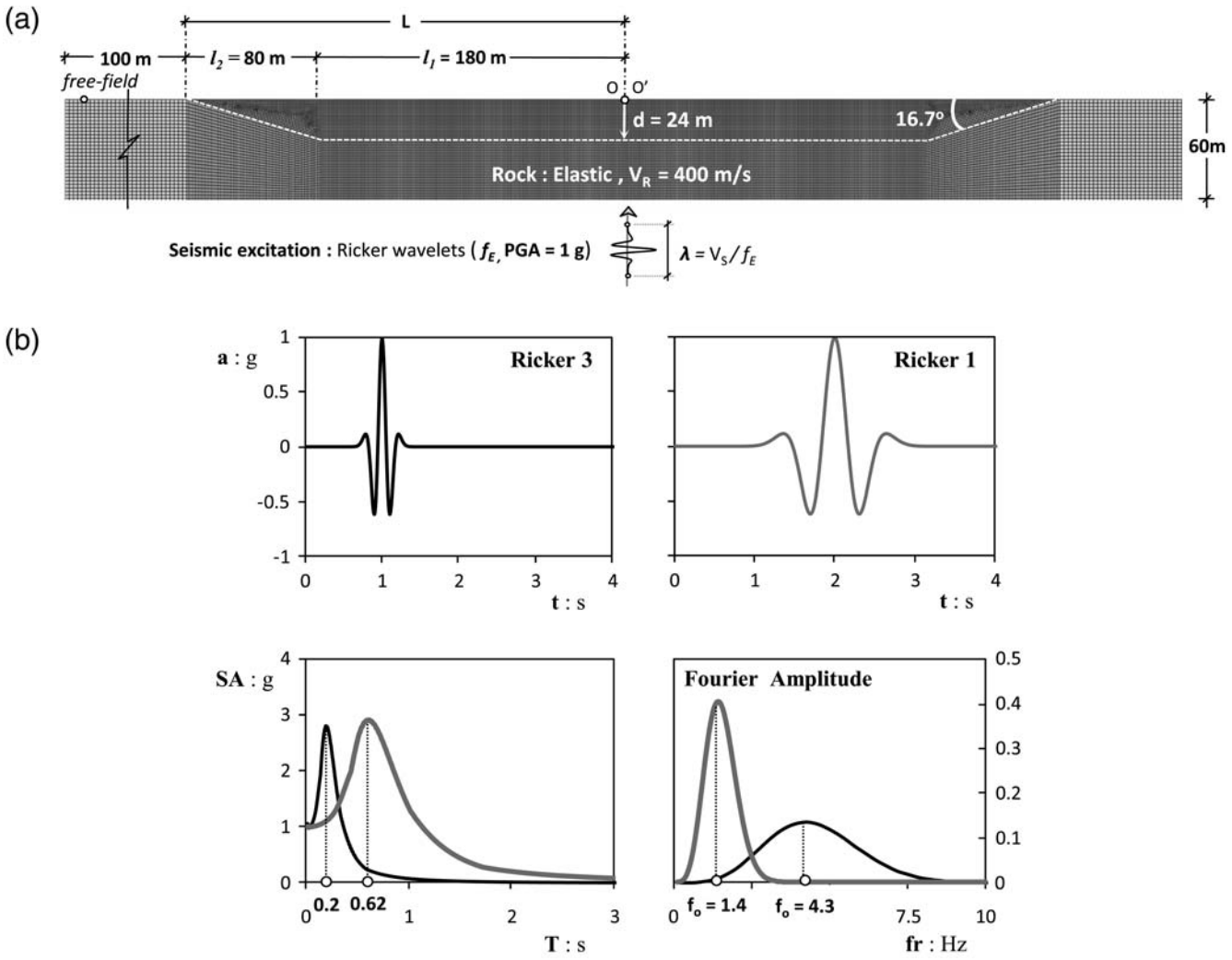

Figure 1. (a) Finite element mesh and key problem parameters. An idealized alluvial valley of width $2L$ and depth d is analyzed in 2D assuming plane strain conditions. Note the very fine discretization inside the valley (minimum element width of less than 1 m). (b) Time histories and the respective response and Fourier spectra of the Ricker wavelets of frequency f_E utilized as seismic excitation for the dynamic time-history analyses of the valley.

well-documented Ohba Valley in Japan (Tazoh *et al.*, 1988, Psarropoulos *et al.*, 1999). The model is excited by two pulses (Ricker, 1960) of different dominant frequency: Ricker 1 of characteristic frequency $f_p = 1.4$ Hz, corresponding to a relatively long period seismic excitation; and Ricker 3 of $f_p = 4.3$ Hz, which is characterized by a much higher frequency content. Ricker pulses are narrow banded and are therefore considered appropriate for bringing the governing trends to light.

Results are mainly presented in the form of spatial distribution along the valley surface as follows:

- Aggravation factor $AG = A_{2D}^H / A_{1D}^H$ (defined as the ratio of the peak value of horizontal acceleration, taking account of 2D effects, over the peak acceleration predicted by 1D analysis of isolated soil columns), and
- Peak value of the parasitically generated vertical component $A_V^{(2D)}$, which is the outcome of the refraction of inclined waves on the valley surface and has been shown to be synchronous and of similar frequency content with the horizontal component A_H, thus being quite detrimental to overlying structures (see Gelagoti *et al.*, 2010). It is needless to note that $A_V^{(1D)} = 0$.

The Effect of Soil Stiffness

The elastic 2D responses of three homogeneous valleys (of the same geometry) are compared, with the shear wave velocity V_S of the soil being the only changing parameter, so as to model (1) a very soft formation of $V_{S1} = 100$ m/s, (2) a moderately soft one of $V_{S2} = 150$ m/s, and (3) a relatively stiff valley of $V_{S3} = 200$ m/s. The shear-wave velocity of the substratum is kept constant and equal to $V_R = 400$ m/s. Thus, the impedance contrast ratio $(\rho_R V_R / \rho_S V_S)$ between the soil ($\rho_S = 1.6$ Mg/m^3) and the underlying rock stratum ($\rho_R = 2.0$ Mg/m^3) ranges from 2.5 to 5.

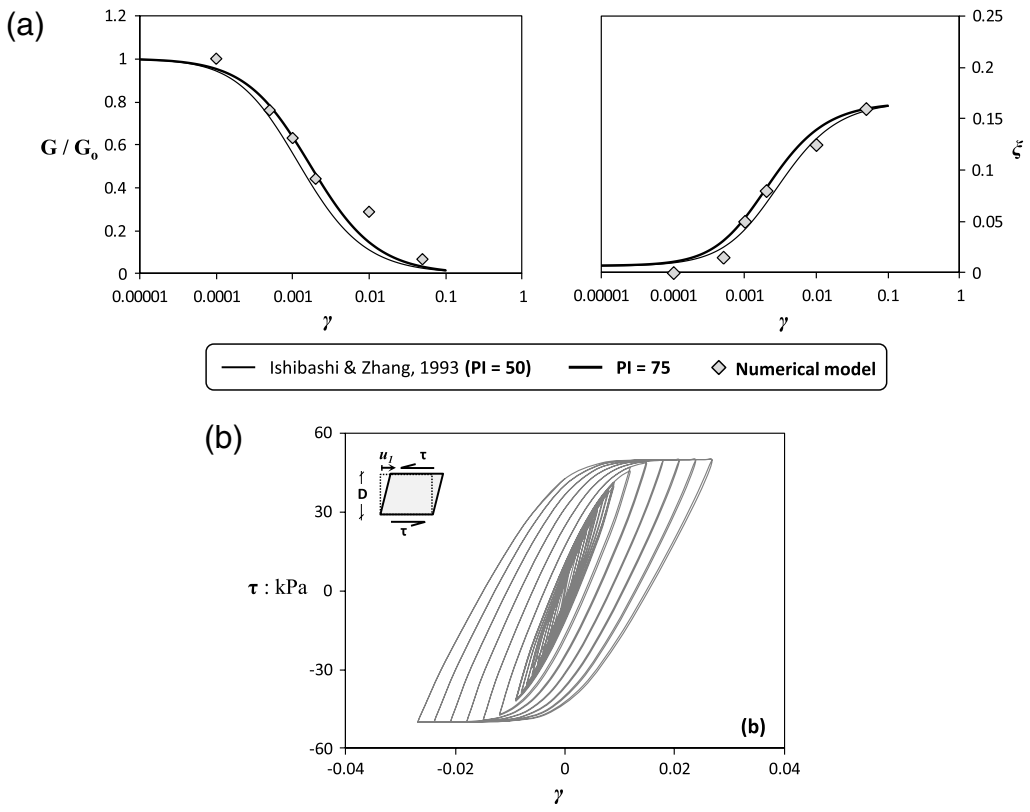

Figure 2. Calibration of the soil numerical model. (a) A comparison of the numerically predicted G/G_o ratio versus shear strain γ and damping ratio ξ versus shear-strain γ curves with published data. (b) An example τ-γ loop produced when a soil element of $S_u = 50$ kPa is subjected to cyclic shear deformation of gradually increasing amplitude.

For the long-period Ricker-1 seismic excitation (scaled at PGA = 1 g), the differences between the two extreme cases (very soft valley, $V_{S1} = 100$ m/s; slightly stiff valley, $V_{S3} = 200$ m/s) can be visualized in Figure 3 in terms of wavefield patterns produced through seismogram synthetics—an illustrative diagnostic tool that may be used to portray the evolution of generated waveforms as they appear on the valley surface. Seismogram synthetics are produced by collocating the ground motion time histories at each point along the valley surface. To this end, the vertical axis of the diagram represents the distance along the valley surface, while the acceleration time histories are plotted along the horizontal axis. In the case of the slightly stiff valley (Fig. 3a), the response is essentially 1D; the imposed shaking reaches almost simultaneously all the points along the valley surface. The signal shows amplitude amplification over the base excitation but a rather negligible increase in duration. Surface waves at $C = 360$ m/s are barely visible on the seismogram synthetics; these waves do not seem to affect the amplitude of motion of the central portion of the basin. In stark contrast, when the softer valley is examined (Fig. 3b), the initial arrivals of *SV* waves are followed by some later arrivals, which should be attributed to Rayleigh waves generated at the valley edges and propagating along its surface. This is reflected on the time histories of A_H recorded at $x = 160$ m: the produced signal on the surface of the $V_S = 100$ m/s soil has a substantially higher duration than the imposed seismic excitation, and the initial strong motion pulse is followed by several weaker (lower amplitude) pulses. The apparent propagation velocity of the late arriving waves is graphically calculated to be equal to $C \approx 220$ m/s, a value which is substantially higher than the wave velocity of 100 m/s, thus confirming that the subsequent pulses have originated from surface waves. Indeed, the value of $C = 220$ m/s for the Ricker-1 pulse with $f_p = 1.4$ Hz, valley depth $d = 24$ m, and $V_S = 100$ m/s gives $2\pi/kd = C/f_o d = 6.5$ and $C/V_S = 2.2$, which are in agreement with the theoretical dispersion curve of Kanai (1951)plotted in Figure 3c for a two-layered half-space with density ratio $\rho_2/\rho_1 = 1$ and $G_2/G_1 = 20$, corresponding to $V_{S2}/V_{S1} = 4.4$, which is approximately our case. Similarly, for the slightly stiff valley, the Rayleigh-wave dispersion curve for a two-layered half-space having $\rho_2/\rho_1 = 1$, $G_2/G_1 = 5$ (approximately our case) gives a velocity value of $C_R = 360$ m/s for $2\pi/kd = 10$.

Such phenomena are also reflected in the spatial distributions of A_H, A_V, and AG along the valley surface (Fig. 4). As revealed by the distribution of peak horizontal acceleration A_H (Fig. 4a), when the $V_{S3} = 200$ m/s valley is excited by the relatively low frequency Ricker-1 pulse, its response is practically 1D. A higher-amplitude response is observed in the central area of the valley, while a smooth transition is observed toward the valley edges, owing to the impedance

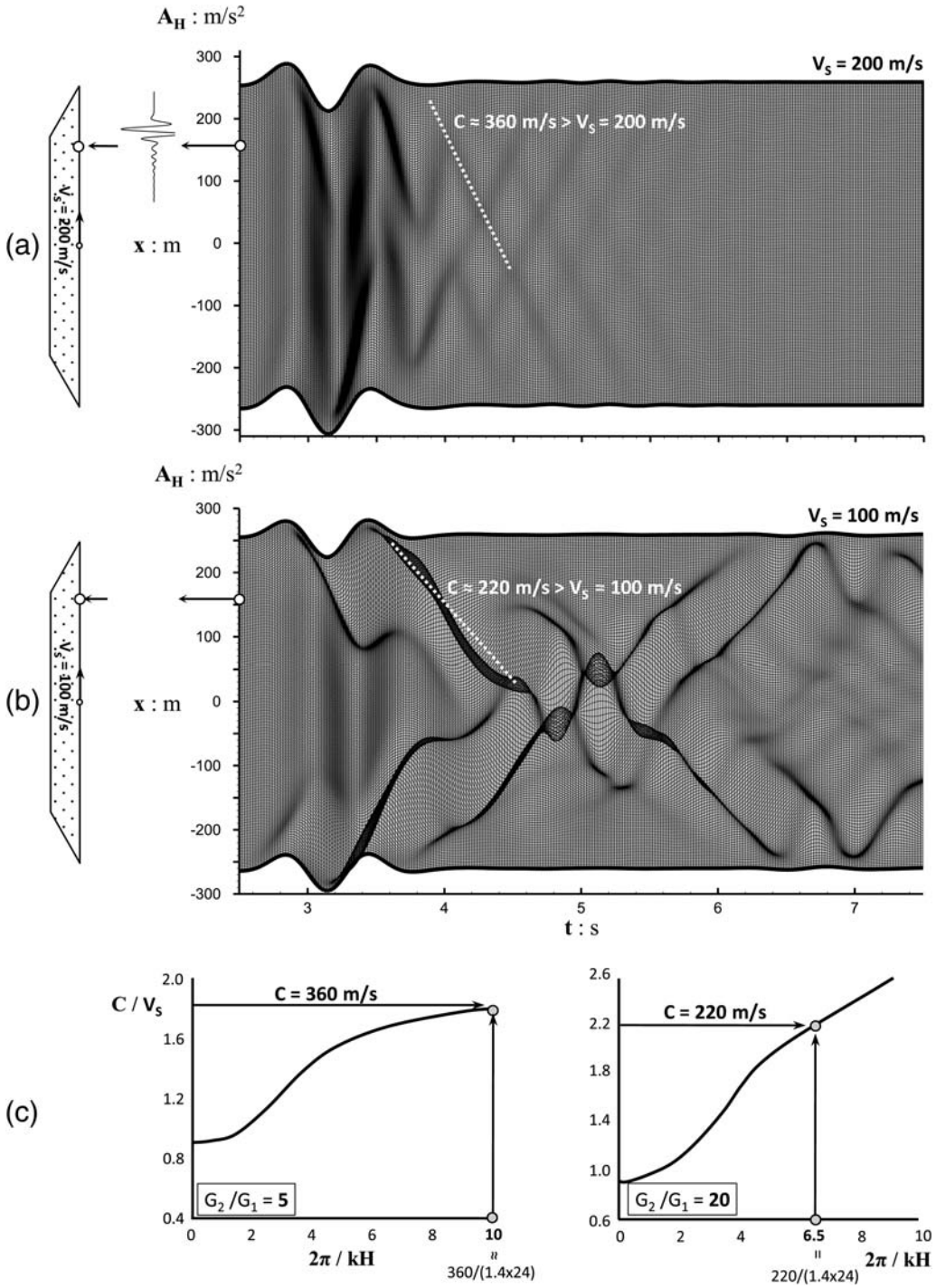

Figure 3. Seismogram synthetics illustrating the effect of shear-wave velocity V_S on the produced wave-field patterns for (a) a stiff valley of $V_S = 200$ m/s and (b) a much softer valley of $V_S = 100$ m/s. Both valleys are excited by a low frequency Ricker-1 pulse ($f_o = 1.4$ Hz), assuming elastic soil response. (c) Validation of the numerically calculated Rayleigh-wave phase velocities in comparison with theoretical dispersion curves of Kanai (1951).

contrast between the soil and the outcropping bedrock. Recall that in the case of the stiff valley the generated wavelengths (defined as the ratio $\lambda = V_S/f$, where f is the dominant frequency of the seismic excitation) are relatively long (ranging from $\lambda \approx 50$ m to $\lambda \approx 200$ m). Hence, it is apparent that the valley geometry, with the largest convex dimension being only 24 m, is inadequate to create any notable wave refractions and generates surface waves leading to $AG \approx 1$ along the whole length of the valley (Fig. 4b). As the valley stiffness reduces to $V_{S2} = 150$ m/s and $V_{S1} = 100$ m/s, the generated wavelengths decrease and the geometry of the valley becomes more perceptible to the incoming

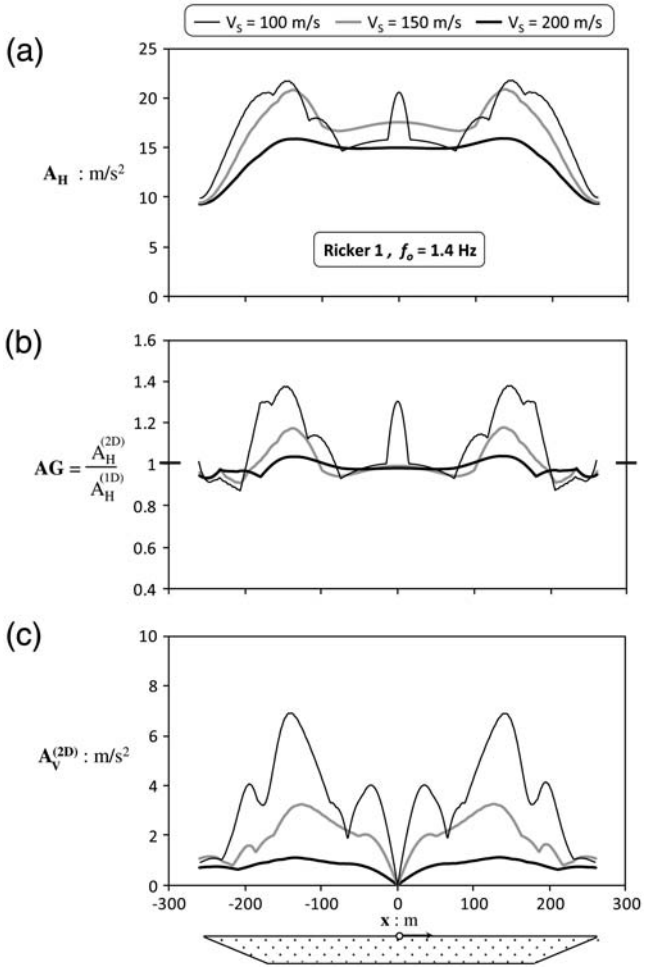

Figure 4. The effect of soil stiffness on the viscoelastic response of the valley subjected to a low-frequency Ricker-1 wavelet. The spatial distribution of (a) horizontal peak ground acceleration A_H, (b) aggravation factor AG, and (c) parasitically generated (due to the 2D geometry) vertical acceleration A_V.

waves. Consequently, 2D valley effects are noticeably enhanced (Fig. 4b). It is noteworthy that for the softer valley ($V_{S1} = 100$ m/s), which generates the larger aggravation AG (i.e., the surface ground motion is amplified by roughly 40% compared to what the 1D theory would predict), valley effects are prominent along many parts on the valley surface. As is clearly manifested in the wave-field pattern of Figure 3, the latter is contaminated by high-amplitude Rayleigh waves. The steep peaks of AG, which mainly appear at the center of the valley and at locations around $x \approx \pm 150$ m, may be attributed to the constructive interference of antithetically propagating Rayleigh waves, or to the interference of Rayleigh waves with vertically propagating SV waves. At intermediate locations $x \approx \pm 50$ m, Rayleigh waves interfere destructively and only the SV (1D) waves produce the motion.

The described phenomena are even more conspicuous in terms of distribution of the parasitic vertical acceleration A_V along the valley surface (Fig. 4c). Since this component is the result of 2D valley geometry, it can practically appear only when the wavelength is adequately small and therefore able to perceive the topographic relief. Thus, when the valley formation is stiff, the lack of refractions results in negligible parasitic vertical acceleration (not exceeding 10% of the amplitude of the purely horizontal seismic excitation). On the other hand, as the soil profile softens, the vertical component is drastically amplified, reaching almost 70% of the horizontal seismic excitation at certain locations.

The aggravation pattern changes radically when the three valleys are excited by the high frequency Ricker-3 wavelet, which generates smaller wavelengths capable of perceiving the topographic relief in greater detail (Fig. 5). Yet, the central part of the valley is (in all three cases) completely oblivious to the quite complex wave-field pattern, and the response in this region does not substantially deviate from the 1D response: $AG \approx 1.2D$ aggravation phenomena are only evident near the valley edges, and tend to amplify with the decrease of shear wave velocity. The maximum AG reaches 1.4 for the softer case of $V_{S1} = 100$ m/s within a quite narrow band near the valley edges, followed by a

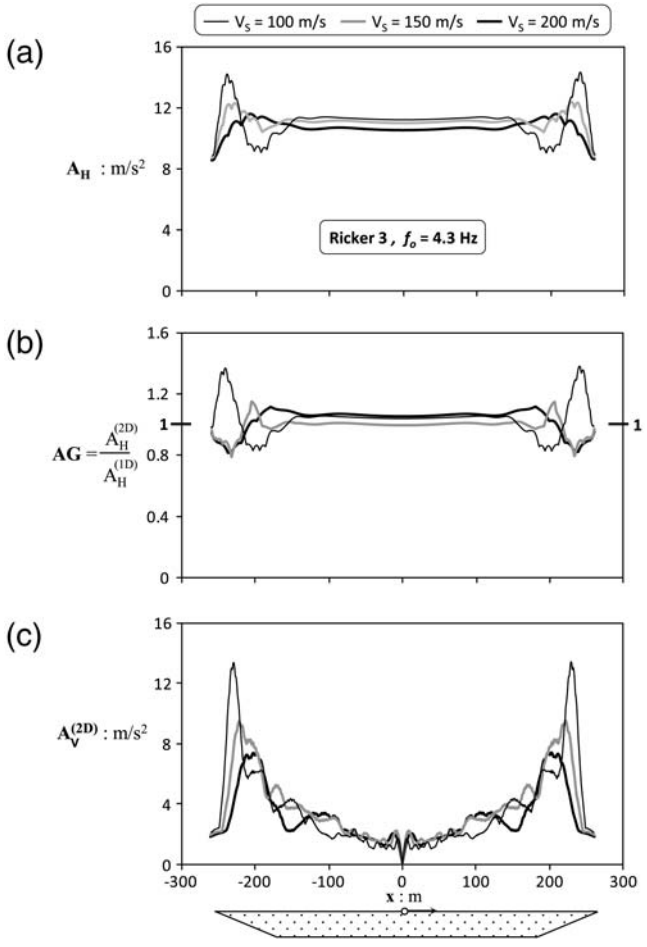

Figure 5. The effect of soil stiffness on the viscoelastic response of the valley subjected to a low-frequency Ricker-3 wavelet. The spatial distribution of (a) horizontal peak ground acceleration A_H, (b) aggravation factor AG, and (c) parasitically generated (due to the 2D geometry) vertical acceleration A_V.

shadow zone where AG falls below 1.0, a deamplification compared to the 1D motion. As the valley soil stiffens ($V_{S2} = 150$ m/s), AG drops to roughly 1.2, while the shadow zone precedes the zone of the peak (i.e., it is now closer to the valley edges, covering much of the surface directly above the valley wedges). Further increase of the shear-wave velocity to $V_{S3} = 200$ m/s results in a further decrease of the intensity of produced valley effects ($AG \approx 1.1$, while the shadow zone remains unchanged, extending along much of the surface above the wedges).

Contrary to the horizontal component, the parasitically generated vertical component A_V reaches surprisingly high values even for the stiffer soil profiles (Fig. 5b). Although the horizontal acceleration is slightly deamplified inside the valley wedges, the vertical component even exceeds 8 m/s^2 (i.e., 80% of the bedrock input motion) in the same areas. The amplitude of the vertical motion is further augmented (becoming as high as 13.5 m/s^2) when the profile becomes softer, but now the high acceleration values are only detectable over a very small length (≈15 m) close to the valley edges. It is noteworthy that the location of the peak valley-generated vertical component gradually shifts toward the valley edges as the shear wave velocity decreases. This shift is again attributed to the geometry of the valley relative to the wavelength of the seismic excitation. As the wavelength decreases (i.e., as V_S decreases), the geometry becomes increasingly more perceptible by the incoming waves, and wave refractions toward the convex borders of the valley wedges are intensified. The entrapment of multiply refracting waves within the valley wedges naturally amplifies the vertical component in those areas, shifting the location of the peak toward the valley edges.

The Effect of Soil Nonlinearity

The effect of soil nonlinearity on 2D valley effects has been extensively examined in the literature with various methods ranging from equivalent linear to fully inelastic analysis (Marsh *et al.*, 1995; Zhang and Papageorgiou, 1996; Pavlenko, 2001; Pergalani *et al.*, 2003; Olsen *et al.*, 2006; Lenti *et al.*, 2009; Gelagoti *et al.*, 2010). Most studies conclude that soil inelasticity reduces 2D valley amplification, and hence AG tends to diminish.

Such a case study is presented in Figure 6, referring to the soft valley formation ($V_S = 100$ m/s and $S_u = 50$ kPa) excited by a high frequency Ricker-3 pulse of PGA = 10 m/s^2. Indeed, soil nonlinearity results in a decrease of 2D soil amplification with AG dropping from 1.4 (for elastic soil response) to 1.2 near valley edges, while the shadow area ($AG < 1$) becomes wider and deeper (Fig. 6a). Similarly beneficial is the role of soil inelasticity in terms of the parasitically generated vertical component A_V (Fig. 6b), which decreases from roughly 14 m/s^2 to 8 m/s^2 while its distribution along the valley surface is only constrained at the wedges.

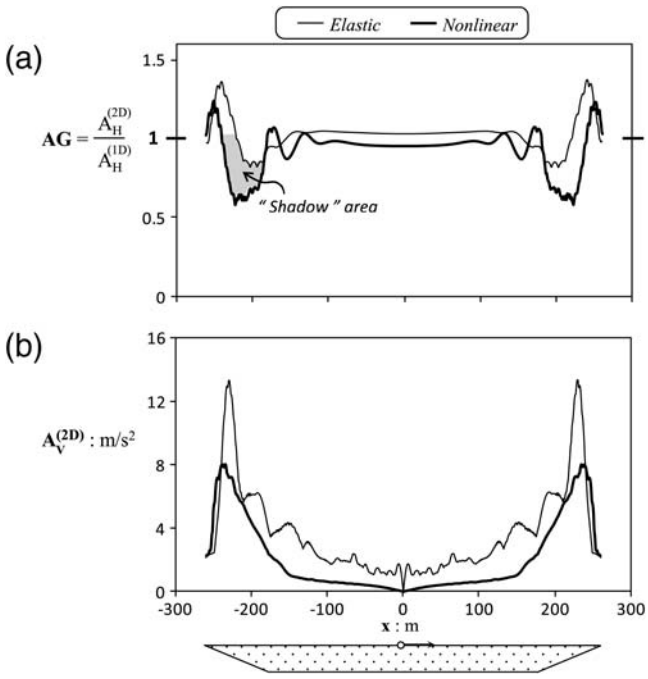

Figure 6. Illustrative example of the beneficial role of soil nonlinearity: a comparison of elastic with nonlinear analysis for a relatively soft valley of $V_S = 100$ m/s and $S_u = 50$ kPa excited by a high-frequency Ricker-3 pulse. The spatial distribution along the valley surface of (a) aggravation factor AG and (b) parasitically generated vertical acceleration A_V.

Yet, soil nonlinearity is not always beneficial. In fact, in some cases it may even become detrimental. Figure 7 depicts one such example, referring to the stiff valley ($V_S = 200$ m/s, $S_u = 150$ kPa) excited by a relatively low frequency pulse (Ricker 1). AG now increases with soil nonlinearity to nearly 1.20 (Fig. 7a). Due to soil plastification, the shear stiffness of the alluvium decreases from G_o (small strain, elastic) to a substantially lower secant value G, corresponding to a lower effective shear-wave velocity $\bar{V}_S$. This decrease produces lower wavelengths and, subsequently, enhances 2D valley effects, compared with the elastic case, where the wavelengths were too long to perceive the geometric irregularity of the bedrock. This mechanism is further elucidated in the spatial distribution of the vertical (parasitic) acceleration A_V (Fig. 7b). The latter is systematically larger in the nonlinear case along the whole valley length, while its maximum value ($A_{V,\max} = 5$ m/s^2) close to valley edges is much higher than in the elastic analysis.

The aforementioned role of soil nonlinearity may be crisply visualized through the produced wave-field patterns. Figure 8 compares the generated waveforms for the two previously discussed extreme cases: (a) a soft valley of $V_S = 100$ m/s and $S_u = 50$ kPa, excited by a high-frequency Ricker-3 pulse, where soil nonlinearity is beneficial (i.e., soil nonlinearity wipes out 2D effects, thus reducing AG); and (b) a rather stiff valley of $V_S = 200$ m/s and

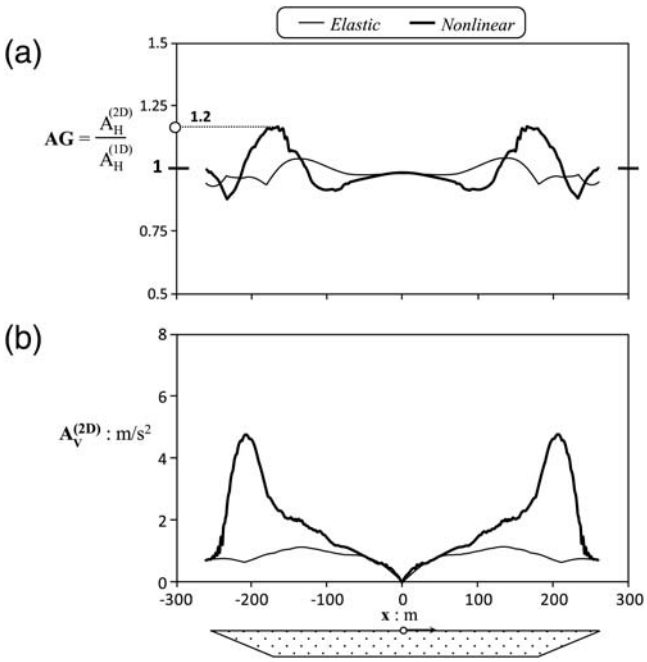

Figure 7. Illustrative example of the detrimental role of soil nonlinearity: a comparison of elastic with nonlinear analysis for a stiff valley of $V_S = 200$ m/s and $S_u = 150$ kPa excited by a relatively low-frequency Ricker-1 pulse. The spatial distribution along the ground surface of (a) aggravation factor AG and (b) parasitically generated vertical acceleration A_V.

$S_u = 150$ kPa subjected to a low-frequency Ricker-1 pulse, where soil nonlinearity is detrimental (i.e., 2D effects are amplified and increasing AG). In the former case (Fig. 8a), the complex wave field of the elastic case (top seismogram) vanishes to a much smoother pattern (bottom seismogram). Evidently, the multiple waveforms and modes of surface waves tend to be damped out as they propagate along the surface. Limited 2D phenomena are only localized close to the valley edges, as indicated by the slight crumpling of the seismogram in that area.

In the latter case (Fig. 8b), the wave field of the elastic case (top seismogram) is quite smooth, revealing an essentially 1D response, as the long-wavelength waves do not distinguish the valley geometry. Ripples of Rayleigh waves are barely distinguishable, and apparently they hardly affect the motion in most of the valley. This picture changes when we account for soil nonlinearity (bottom diagram). As already discussed, soil plastification reduces the effective shear modulus of the soil and thereby the produced wavelengths, hence the waves become more sensitive to the lateral heterogeneity of the bedrock, which is now more easily perceptible (white dashed line in the figure). The generation of Rayleigh waves may also be noticed. However, being highly damped due to inelastic soil response, they are unable to produce significant amplification.

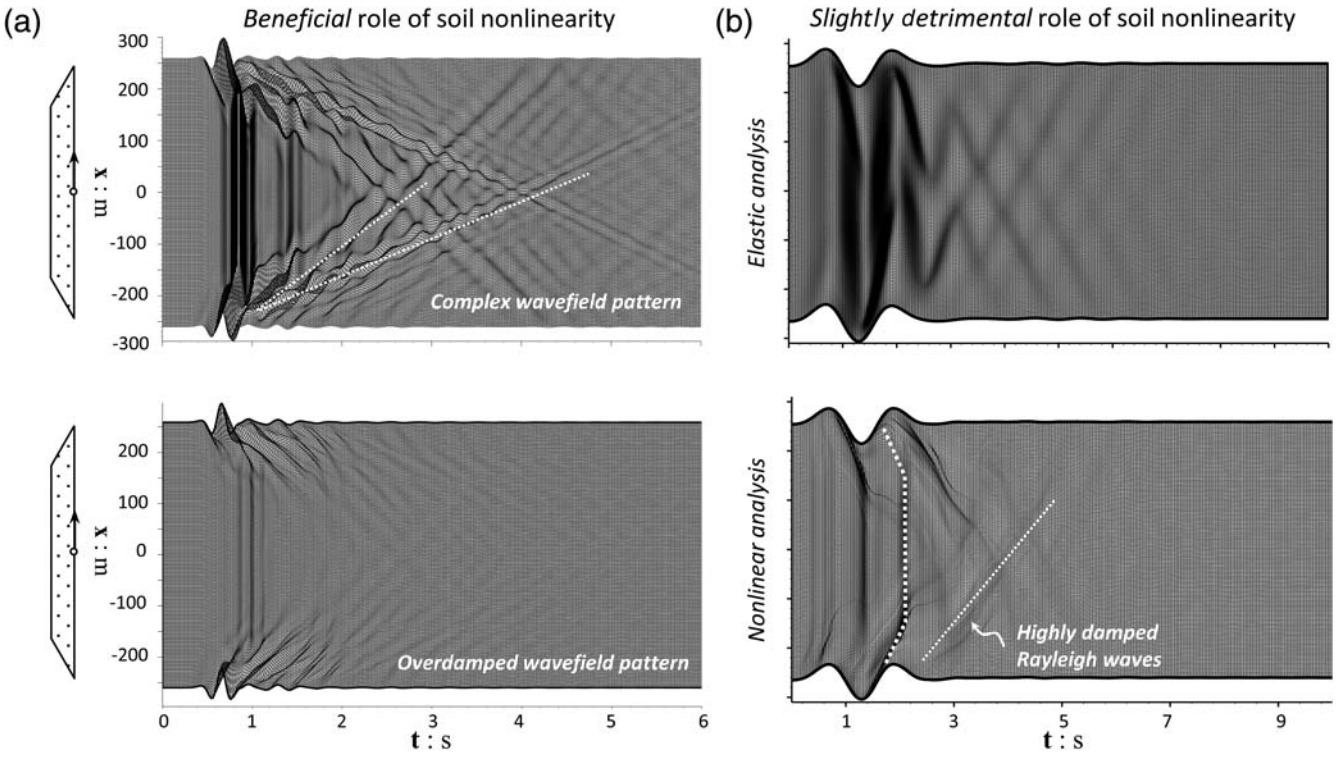

Figure 8. Illustration of the role of soil nonlinearity in terms of horizontal acceleration wave fields. A comparison of elastic (top row) with nonlinear analysis (bottom row) for (a) a soft valley of $V_S = 100$ m/s excited by a high-frequency Ricker-3 pulse, where soil nonlinearity is beneficial, and (b) a rather stiff valley of $V_S = 200$ m/s subjected to a low-frequency Ricker-1 pulse, where soil nonlinearity is detrimental.

Dimensional Analysis

The preceding analysis has highlighted the sensitivity of 2D valley response to a variety of key problem parameters, elucidating the need for dimensional analysis. In this section we attempt to perform a formal dimensional analysis (Langhaar, 1951) of the dynamic response of 2D valley formations.

Generation of Nondimensional Terms

Dimensional analysis may be thought of as a mathematical process that outlines the major mathematical expressions describing natural phenomena. According to Makris and Black (2004), the application of dimensional analysis to any particular physical phenomenon is based on the premise that the phenomenon can be described by a dimensionally homogeneous equation that relates the dependent variables u_1 and the independent variables $u_2, \ldots, u_k$ as

$$u_1 = f(u_2, u_3, \ldots . u_k). \tag{6}$$

In this context, for the case of an homogeneous alluvial valley, and taking account of soil nonlinearity, it is expected that the ground accelerations at the valley surface, A_H and A_V, and the associated aggravation factor AG, will be a function of the following:

- Valley geometry, expressed through its half-length L and depth d (see Fig. 1),
- Elastic properties of the soil, expressed through its density ρ_S and shear wave velocity V_S, and of the underlying bedrock, expressed through ρ_R and V_R,
- Prefailure nonlinear soil properties G-γ and ξ-γ,
- Soil strength, expressed through the undrained shear strength S_u, and
- Seismic excitation characteristics, expressed through the pulse amplitude a_p and dominant frequency f_p, or dominant period T_p.

For the sake of simplicity, the formulation presented in the ensuing discussion refers to homogeneous alluvial clayey deposits of uniform S_u, constant angle $\theta = 16.7°$, and elastic bedrock response. Source effects influencing the inclination and type of incoming waves are not taken into account; excitation is only vertically propagating *SV* waves. The analysis presented is conducted on the basis of Ricker pulses, which may be described by a single characteristic frequency.

Based on the previous formulation, the response at the valley surface (i.e., A_H and A_V; AG) will be a function of

$$AG, A_H, A_V = f(d, L, V_S, V_R, \rho_s, \rho_R, S_u, a_p, T_p, \theta). \tag{7}$$

Apparently, this equation contains $k = 11$ independent variables that, given its homogeneous dimensionality, may be reduced to a smaller number of dimensionless terms defined as Π-terms (Barenblatt, 1996). Indeed, following the Vaschy–Buckingham Π-theorem, a dimensionally homogeneous equation involving $k$variables may be transformed to a function of k-r dimensionless Π-products, where r is the minimum number of reference dimensions necessary for the description of the physical variables. In the specific problem, the 10 physical variables can be described by three reference dimensions: mass (M), time (T), and length (L). Therefore the dimensionless form of equation 6 will include $11 - 3 = 8$ Π terms.

Consequently, and obeying the aforementioned principles, equation 7 may be rearranged as follows:

$$AG, A_H/a_p, A_V/a_p = f(i, \lambda_S, \lambda_R, v, \rho, s, \theta), \tag{8}$$

where θ is the angle of the inclined boundary of the valley, and

$$i = \rho_R V_R / \rho_S V_S \tag{9}$$

is defined as the impedance ratio between the soil and the surrounding rock. Accordingly, the normalized wavelengths λ_S and λ_R within the valley soil and the bedrock, respectively, are defined as

$$\lambda_S = V_S / f_p d, \tag{10}$$

and

$$\lambda_R = V_R / f_p d. \tag{11}$$

Physically, the dimensionless wavelength λ can be seen as an index of the ability of the generated waves to capture the valley geometry. Hence, small λ values are indicative of small wavelengths, relative to the valley dimensions, which in turn results in a more perceptible valley geometry and therefore increased number of wave reflections. The term λ_S may equivalently be regarded as one fourth of the ratio of the dominant period of the excitation pulse over the soil natural period.

Soil nonlinearity is expressed through a dimensionless term r, named hereafter shear resistance ratio, which is defined as

$$r = S_u / \rho_s d \alpha_p, \tag{12}$$

in which S_u is the available shear strength and $\rho_s d \alpha_p$ is an index of the earthquake-induced stress at depth d. In other words, r may be considered as an index of the mobilization of soil shear strength.

The valley shape is defined with the ratio s of the valley length over its depth,

$$s = L/d, \tag{13}$$

and the tangent of the angle of the wedge $\tan\theta$. (Note that if the valley was sufficiently wide, the wedge angle θ alone would be enough to describe the valley geometry).

Finally, the factor

$$v = \rho V_S^2 / S_u, \tag{14}$$

termed rigidity ratio in soil mechanics literature, is the ratio of the soil shear modulus (at small strains) over the undrained shear strength.

The ultimate scope of dimensional analysis will be the production of self-similar results (i.e., results obeying a special type of symmetry, which is invariant with respect to scale or size transformations [Makris and Black, 2004]). In the sequel, the self-similarity in the response of a number of example valleys is investigated to verify the formulation presented herein. According to the previously stated dimensional analysis, despite the different characteristics of the analyzed valleys, their response should be self-similar, provided that the equality of nondimensional terms is maintained. The valley geometries and the excitation time histories utilized to confirm the aforementioned allegation are summarized in Tables 1 and 2, considering elastic and nonlinear soil response, respectively.

Table 1
Properties of the Three Example Valleys Used to Illustrate the Effectiveness of the Dimensional Formulation When Assuming Elastic Soil Response

Variables	Valley A	Valley B	Valley C
Physical Variables			
L (m)	260	360	520
D (m)	24	36	48
$\tan\theta$	0.3	0.3	0.3
ρ_S (tn/m^3)	1.8	1.8	1.8
ρ_R (tn/m^3)	2.3	2.3	2.3
V_S (m/s)	140	180	168
V_R (m/s)	400	514	480
f_p (Hz)	1.0	0.86	0.6
Nondimensional Variables			
$i = \rho_R V_R / \rho_S V_S$	3.70	3.70	3.70
$\lambda_R = V_R / f_p d$	16.67	16.67	16.67
$\lambda_S = V_S / f_p d$	5.83	5.83	5.83
$s = L/d$	10.83	10.83	10.83
$\tan\theta$	0.3	0.3	0.3

Table 2
Properties of the Two Example Valleys Used to Illustrate the Effectiveness of the Dimensional Formulation When Accounting for Nonlinear Soil Behavior

Variables	Valley D	Valley E
Physical Variables		
L (m)	260	520
d (m)	24	48
$\tan\theta$	0.3	0.3
ρ_S (tn/m^3)	1.8	1.8
ρ_R (tn/m^3)	2.3	2.3
V_S (m/s)	99	140
V_R (m/s)	400	566
S_u (kPa)	42.5	85
f_p (Hz)	0.707	0.5
a_p (m/s^2)	10	10
Nondimensional Variables		
$i = \rho_R V_R / \rho_S V_S$	5.15	5.15
$\lambda_R = V_R / f_p d$	23.58	23.58
$\lambda_S = V_S / f_p d$	5.83	5.83
$r = S_u / \rho_S d \alpha_p$	0.1	0.1
$s = L/d$	10.83	10.83
$\tan\theta$	0.3	0.3
$v = \rho_S V_S^2 / S_u$	415	415

Numerical Verification

The effectiveness of the dimensional formulation is first shown for elastic soil response, a case which involves a smaller number of dimensionless terms and is thus simpler for use as an elucidating example. For this purpose, the three equivalent valleys of Table 1 are analyzed. In the elastic problem, dimensionless results can be obtained if the shape indices s and $\tan\theta$ and the wavelength ratios λ_S and λ_R are kept constant. This implies that the ratio of the dominant excitation period T_p over the dominant shear period T_s of the soil profile should be held constant, which enables capturing both the effect of wave propagation and 1D soil amplification. Figure 9 compares the response of the three equivalent valleys of Table 1 with dimensionless parameters ($i = 0.27$, $\lambda_S = 5.83$, $\lambda_R = 16.67$, $s = 10.83$, and $\tan\theta = 16.7°$) in terms of the spatial distribution of dimensionless maximum horizontal A_H/a_p and vertical A_V/a_p acceleration along the valley surface (Fig. 9a) and dimensionless horizontal and vertical acceleration time histories at location $x/l_1 = -0.7$. The self-similarity of the produced curves is evident in all plots.

A similar comparison is performed in Figure 10 for the fully nonlinear problem through analysis of the two equivalent valleys of Table 2 with dimensionless parameters $i = 5.15$, $\lambda_R = 23.58$, $\lambda_S = 5.83$, $r = 0.098$, $s = 10.83$, and $v = 415$. The effectiveness of the dimensional formulation is thus also confirmed for this fully nonlinear problem.

Parametric Analysis

Having verified the effectiveness of the dimensional formulation, a parametric study is conducted to gain insight into the effect of the previously introduced dimensionless parameters on the dynamic response of trapezoidal valleys. Both elastic and nonlinear soil response are considered.

The Effect of Shape Factor

Elastic Soil Response. Three valley geometries are examined (Fig. 11). The central part of the formation, denoted as quasi 1D formation, is exactly the same in all three cases. Consequently, the depth of all valleys is kept constant

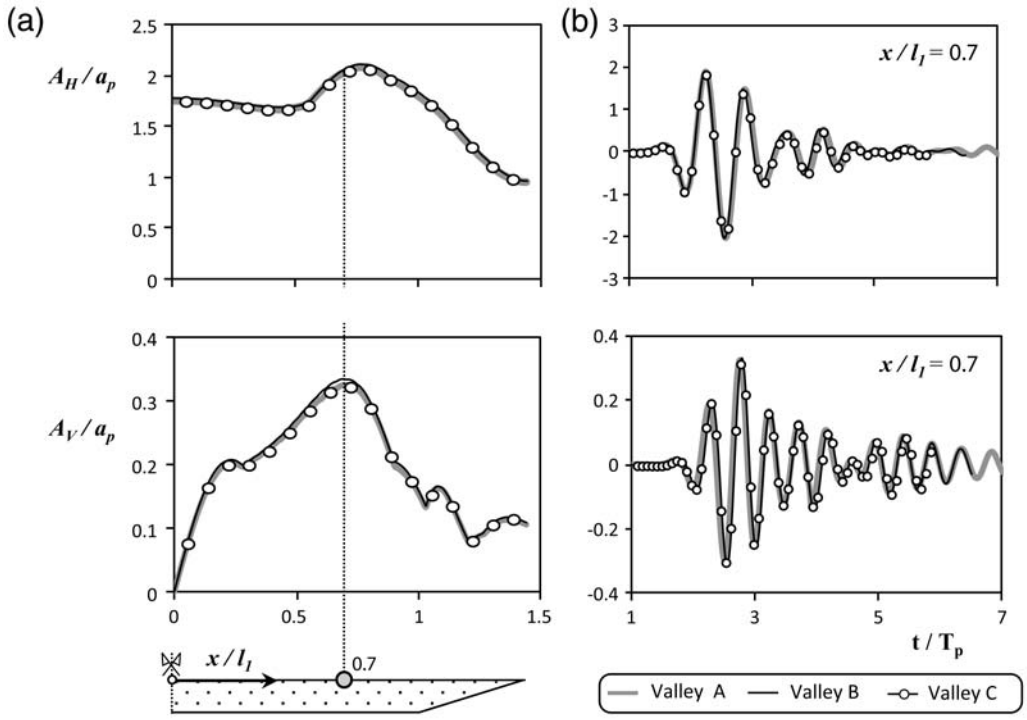

Figure 9. Numerical verification of the dimensional analysis formulation for elastic soil conditions. A comparison of the response of the three equivalent valleys (see Table 1) in terms of (a) spatial distribution of dimensionless maximum horizontal A_H/a_p (top row) and vertical A_V/a_p acceleration (bottom row) along the valley surface, and (b) dimensionless horizontal (top) and vertical acceleration (bottom) time histories at location $x/l_1 = 0.7$.

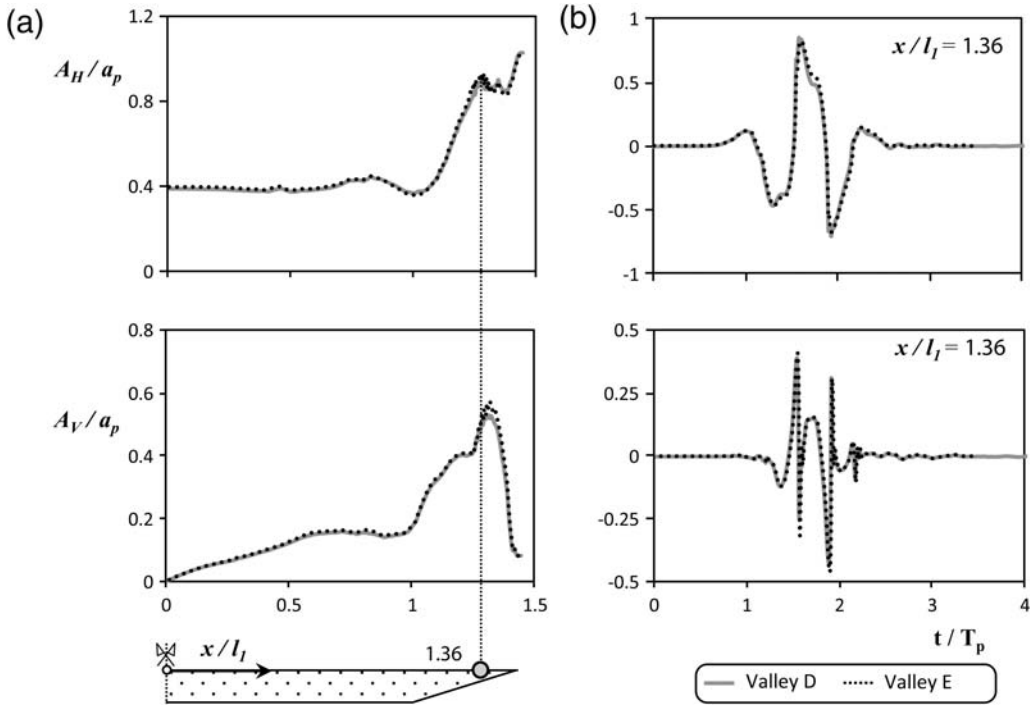

Figure 10. Numerical verification of the dimensional analysis formulation for nonlinear soil conditions. A comparison of the response of two equivalent valleys (see Table 2) in terms of (a) spatial distribution of dimensionless maximum horizontal A_H/a_p (top) and vertical A_V/a_p acceleration (bottom) along the valley surface, and (b) dimensionless horizontal (top) and vertical acceleration (bottom) time histories at location $x/l_1 = -1.36$.

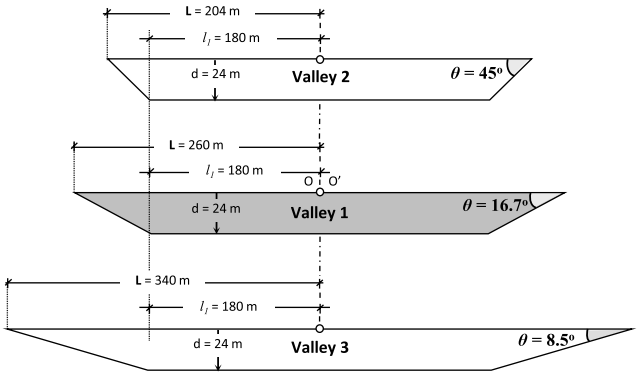

Figure 11. Investigation of the effect of shape factor s: geometric characteristics of the three valley typologies examined. The base case valley 1 has the same geometry as the Ohba Valley (Tazoh *et al*, 1988; Gelagoti *et al*, 2010), valley 2 corresponds to a steeper basin, and valley 3 corresponds to a milder basin. (For the sake of clarity the vertical scale is exaggerated.)

($d = 24$ m). The inclination θ of the wedge boundary, and hence the length of the wedges, is varied parametrically. The geometry of valley 1 (shown in the middle) is inspired by the Ohba Valley in Japan (Tazoh *et al.*, 1988). The inclination of its slopping boundary is considered typical for a number of actual alluvial deposits such as the Ubaye Valley in the French Alps (Jongmans and Campillo, 1993), the Coachella Valley in California (Bodin *et al*, 1994; Rymer, 2000), and the Caracas Valley in Venezuella (Papageorgiou and Kim, 1991). Valleys 2 (top) and 3 (bottom) represent a significantly steeper and a milder formation, respectively. The Rhone Valley and the San Jose, California, basin (Frischknecht *et al.*, 2005; Hartzell *et al.*, 2003) are well-known steep basins similar to the geometry of valley 2. valley 3 may be crudely considered as representative of the Volvi basin in northern Greece (Jongmans *et al.*, 1998), the Marina District basin in California (Hanks and Brady, 1991; Zhang and Papageorgiou, 1996), the Parkway Valley in New Zealand (Chávez-García *et al.*, 1999), the Ashihara Valley in Japan (Kudo *et al.*, 1988; Kawase and Sato, 1992), and the Salt Lake Valley (Benz and Smith, 1998).

As stated previously, when the valley is excited by small wavelengths ($\lambda_S \approx 1$), 2D phenomena are mainly a product of wave reflections in the inclined edges. As is schematically illustrated in Figure 12a for the case of a very gentle valley ($\theta \ll 45°$), the aggravation is expected to be larger, because the geometry of the mild slope allows the generation of numerous reflections within the wedge and subsequently enhances the possibility of constructive wave interferences on the valley surface. This possibility is directly related to the density of wave reflections, which decreases with the distance between consecutive arrivals of reflected waves on

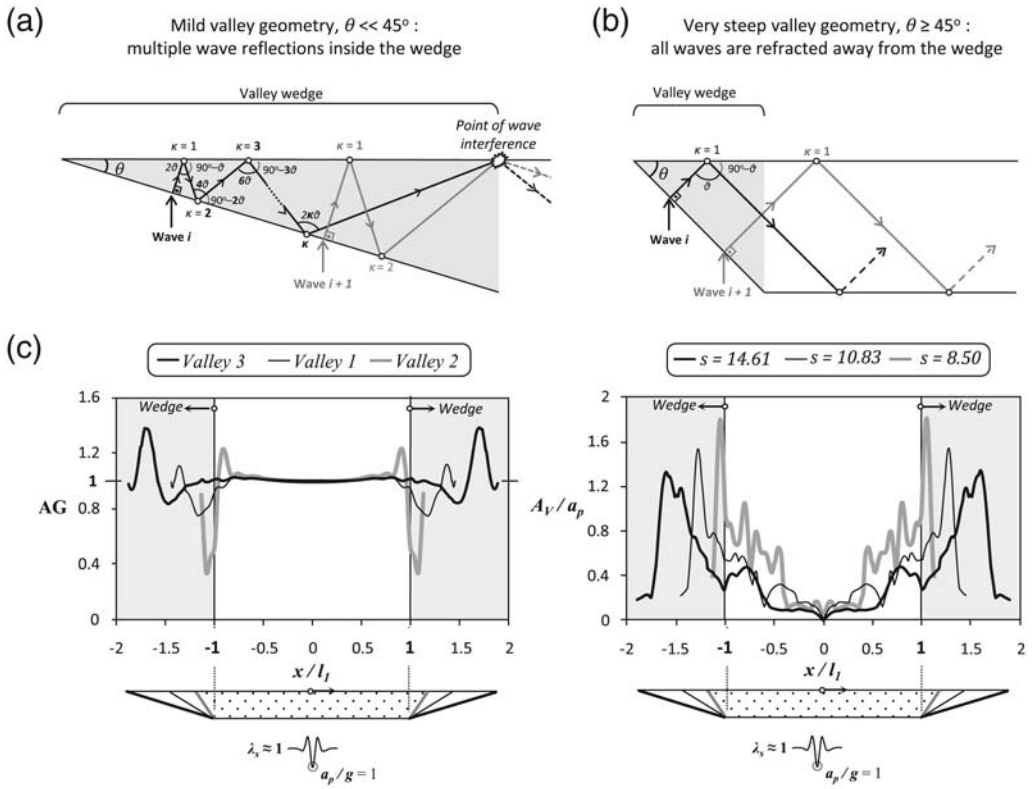

Figure 12. Schematic illustration of the mechanism of wave interference: (a) inside a mild valley of $\theta \ll 45°$, where multiple wave reflections inside the valley wedge are possible, leading to possible interferences inside the wedge; (b) inside a steep valley of $\theta \geq 45°$, where all waves are refracted away from the wedge leading to a lack of focusing effects within the wedge. (c) The effect of shape factor s on the spatial distribution of AG and A_V/a_p along the valley surface for $\lambda_S \approx 1$ (i.e., relatively short wavelength and high frequency) seismic excitation, assuming a viscoelastic soil response.

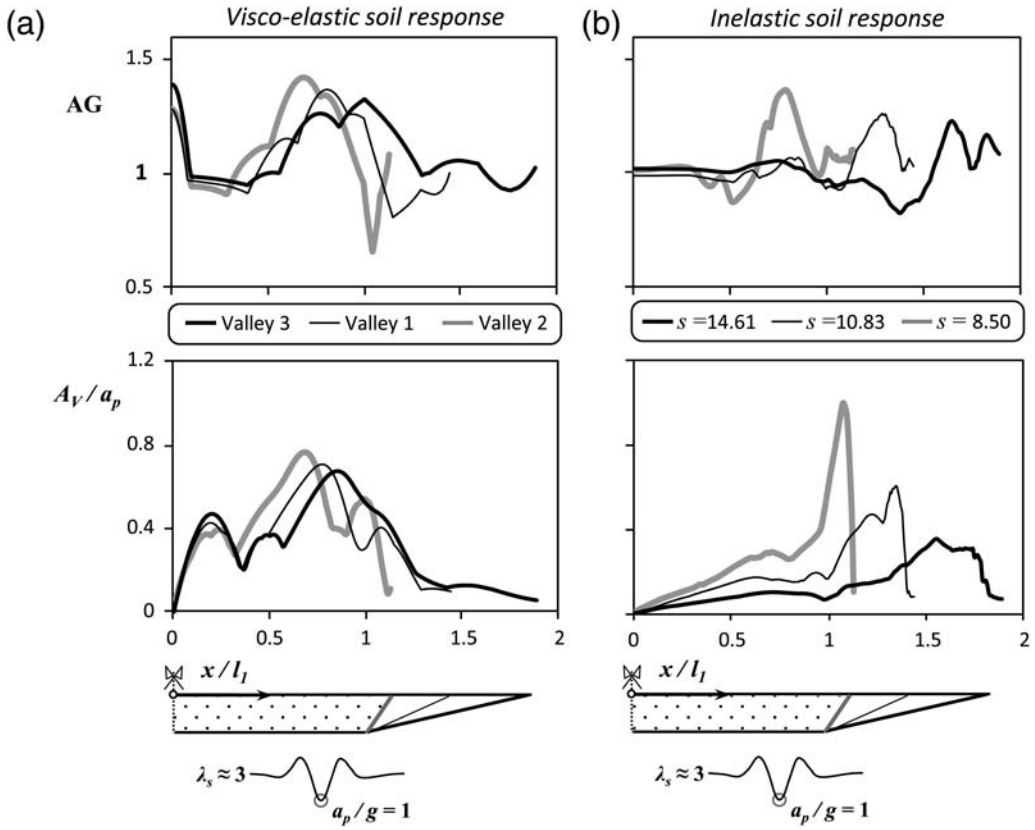

Figure 13. The effect of shape factor s on the spatial distribution of AG (top) and A_V/a_p (bottom) along the valley surface for $\lambda_S \approx 3$ (i.e., relatively long wavelength) excitation: (a) viscoelastic soil; (b) inelastic soil ($a_p/g = 1$).

the valley surface. For a given valley inclination, this distance increases away from the edges of the valley, and therefore the probability of wave interference is reduced. As a result, aggravation is expected to take place close to the valley edges.

In stark contrast, in the case of a steep valley ($\theta \geq 45°$), the prevailing mechanism of wave interference is modified. As shown in Figure 12b, due to the sharp slope inclination, all incoming waves are refracted away from the wedge toward the central part of the valley. Because it is now geometrically impossible for any interference to take place within the valley wedges, aggravation close to the valley edges should not be expected. Additionally, due to the steep valley slope, incoming waves will be deflected to reach the surface significantly inclined; hence, the amplitude of the horizontal component of motion on the valley surface will be a fraction of the total motion amplitude because part of it will be converted to vertical motion. (For $\theta = 45°$ [valley 2], the horizontal input motion A will reach the surface inclined at 45° leading to a horizontal component on the soil surface $A_H = A\cos(45°) \approx 0.7A$, equal to the vertical component A_V.) Consequently, deamplification should be expected within the wedges.

These physical arguments are confirmed by the distribution of AG along the surface of the three valleys (Fig. 12c). In the case of the mild valley 3, the maximum aggravation (1.36) is observed very close to the valley edges. In stark contrast, in the case of the steeper valley 2 ($\theta = 45°$), very limited aggravation is observed within a narrow zone immediately after the wedge ($0.9 < x/l_1 \leq 1$), due to waves being refracted toward the valley center. A quite pronounced shadow zone is observed with the valley wedges, with AG falling even below 0.4. As previously discussed, from a strictly geometric point of view, AG should not exceed 0.7 (the horizontal motion A_H at the valley surface is roughly 70% of the input seismic excitation A).

This behavior (i.e., the development of the shadow zone) fades away as the slope of the wedge boundary becomes gentler. Indeed, in the case of the milder valley 3, limited deamplification is observed only within a very narrow zone inside the wedge. The behavior of valley 1, whose inclination may be characterized as intermediate, falls between the two extremes of valleys 2 and 3.

For the vertical acceleration component A_V/a_p, two main conclusions can be drawn. Unsurprisingly, the peak value of the vertical component $A_{V,\max}$, which is a direct outcome of valley geometry, increases with valley inclination. Especially for the case of the steep valley 3, a noticeable vertical component is observed along a rather extended area within its main body: a clear deviation from a purely 1D response.

All the aforementioned phenomena are substantially less pronounced when the valleys are excited by longer ($\lambda_S \approx 3$)

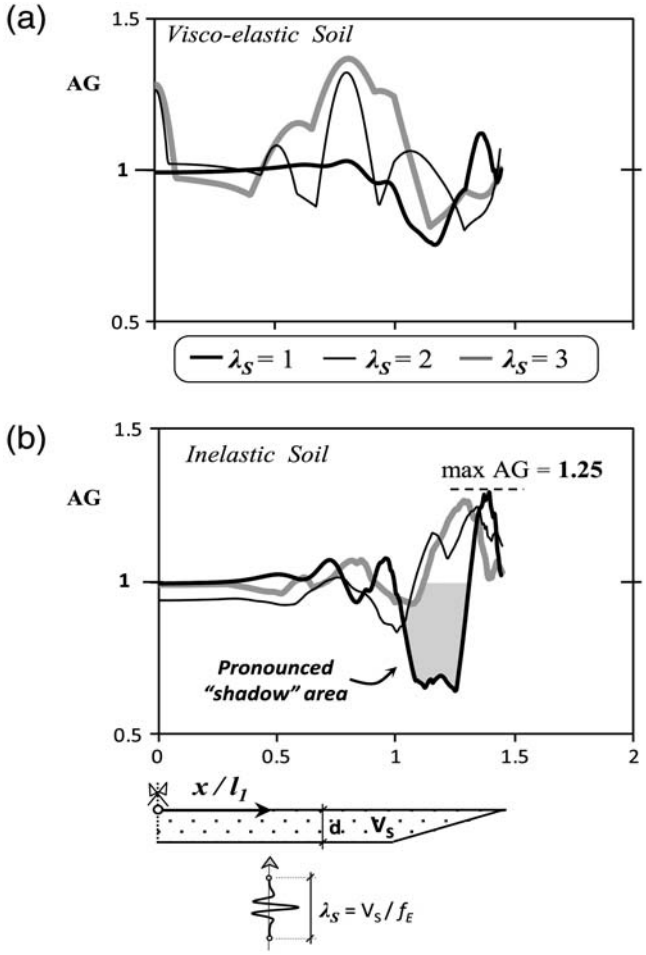

Figure 14. The effect of the dimensionless wavelength ratio λ_S on the spatial distribution of the aggravation factor AG: (a) viscoelastic soil; (b) inelastic soil ($a_p/g = 1$, $r = 0.1$).

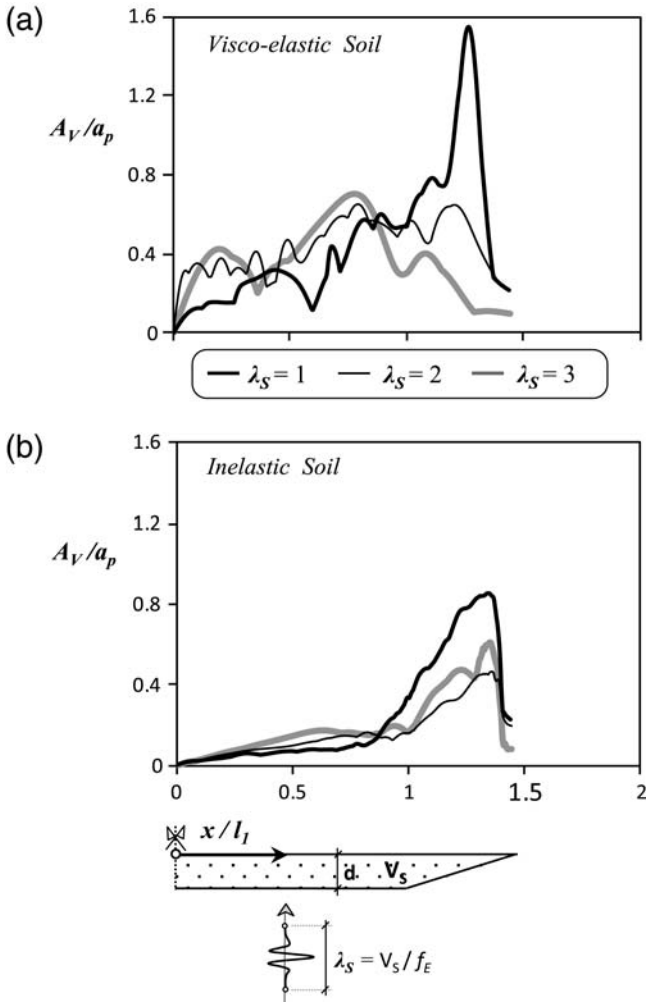

Figure 15. The effect of dimensionless wavelength ratio λ_S on the spatial distribution of the dimensionless maximum parasitically generated vertical acceleration A_V/a_p: (a) viscoelastic soil; (b) inelastic soil ($a_p/g = 1$, $r = 0.1$).

wavelengths (Fig. 13). Assuming elastic soil response (Fig. 13a), the distribution of AG along the valley surface demonstrates a rather common pattern for all cases: 2D amplification is now mostly attributable to surface waves instead of wave focusing effects, rendering the response less sensitive to the valley inclination. The most noteworthy deamplification is observed within the wedge of the steep valley 2, owing to the reasons explained previously. In stark contrast, an almost negligible deamplification is observed in the mild valley 3. Similarly, since in this case the vertical component is also a result of surface waves instead of wave focusing effects, as was the case for $\lambda_S \approx 1$, its distribution and maximum value is quite insensitive to the valley geometry.

Nonlinear Response. When inelastic soil behavior is taken into account ($r = 0.098$, $v = 415$), the amplification mechanisms are modified and aggravation is generally depressed (Fig. 13b). The aggravation peaks of the three valleys are now well separated, and their location has moved toward the edges of the valleys compared with the elastic case. This is attributable to the fact that the multiple reflections that, in the elastic case, were more severe for the milder valley 3 (due to the geometry-induced longer travelling distance) tend to vanish due to soil nonlinearity. Rayleigh waves attenuate as they travel toward the valley center, where now purely 1D response ($AG \approx 1$) is established. 2D phenomena are only contained close to the edges. In terms of the vertical (parasitic) component, the differences among the three valley geometries are quite pronounced. This behavior has its justification in the origin of the vertical acceleration component, which unlike the elastic case is now mainly a product of wave focusing effects near the valley edges rather than surface waves, which now quickly dissipate due to soil inelasticity. The amplitude of A_V/a_p tends to be proportional to the valley inclination, reaching one in the steeper valley 2.

The Effect of Wavelength Ratio λ_S

Figure 14 portrays the effect of λ_S on the distribution of AG along the valley surface, considering viscoelastic and

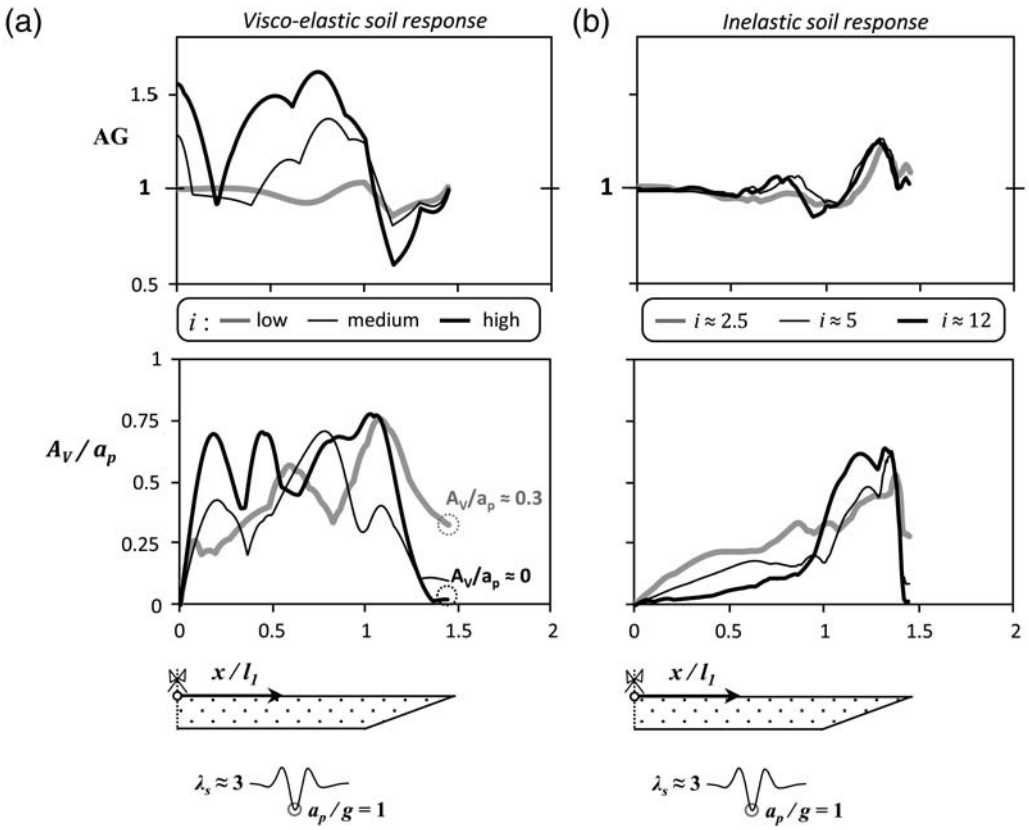

Figure 16. The effect of impedance ratio i on the spatial distribution of AG (top) and A_V/a_p (bottom) along the valley surface: (a) assuming viscoelastic soil response; (b) accounting for nonlinear soil behavior ($a_p/g = 1$, $r = 0.1$).

inelastic soil response. For this purpose, a valley of $i = 5$, $s = 10.83$, $\tan\theta = 0.3$, $r = 0.1$, and $v = 415$ is subjected to three different Ricker excitations of $\lambda_S = 1$, 2, and 3.

With elastic soil (Fig. 14a), when the wavelength ratio is high ($\lambda_S = 3$), the generation of Rayleigh waves is responsible for the significant aggravation (AG reaching 1.2 to 1.4) that is observed along a substantial portion of the valley. As the wavelength reduces ($\lambda_S = 2$) the geometric anomaly is perceived in more detail, leading to a rather volatile aggravation pattern: steep AG peaks followed by shadow areas become detectable along the whole surface of the formation, while conspicuously different aggravation may be distinguished even in adjacent areas along the valley surface. Lastly, as the wavelength reduces further ($\lambda_S = 1$), all 2D amplification phenomena are localized near the very edges of the valley in the immediate vicinity of the triangular wedges. Note that the produced aggravation does not exceed a mere 1.1, while the shadow areas become deeper ($AG_{\min} \approx 0.75$) and wider, extending to even more than half the length of the wedge. The response becomes practically 1D (i.e., $AG \approx 1$) toward the central part of the valley.

On the other hand, when soil nonlinearity is taken into account (Fig. 14b), the aggravation along most of the valley surface is negligible regardless of λ_S: AG reaches a maximum on the order of 1.25 in the vicinity of the valley edges for all wavelengths examined. The only notable effect of λ_S is on the width of the shadow zone, which is much more pronounced ($AG_{\min} \approx 0.65$) for the high frequency seismic excitation ($\lambda_S = 1$).

The effect of λ_S on the dimensionless vertical component A_V/a_p is depicted in Figure 15. Under elastic conditions (Fig. 15a), reducing λ_S produces more complex waveforms, thus bringing about a quite abrupt distribution of peak vertical accelerations A_V/a_p along the valley surface. More importantly, lower λ_S values are responsible for the reduction of A_V/a_p in the central part of the valley. This concentration of significant vertical acceleration ($A_V \approx 1.67a_p$) is the outcome of multiple wave reflections at the inclined boundaries. Larger wavelength excitations ($\lambda_S = 2$ and 3) on the other hand, creating mainly Rayleigh waves at the edges, lead to fairly uniform vertical acceleration along the valley center. However, when soil nonlinearity is considered (Fig. 15b), the distribution of A_V/a_p becomes practically insensitive to λ_S: the maximum A_V/a_p is always observed close to valley edges, almost disappearing from the valley center and, for the short wavelength $\lambda_S = 1$, is reduced to half of its peak elastic value.

The Effect of Impedance Ratio i

The effect of the impedance ratio $i = \rho_R V_R/\rho_S V_S$ in the distribution of AG and A_V/a_p along the valley surface is depicted in Figure 16 referring to a valley of $s = 10.83$,

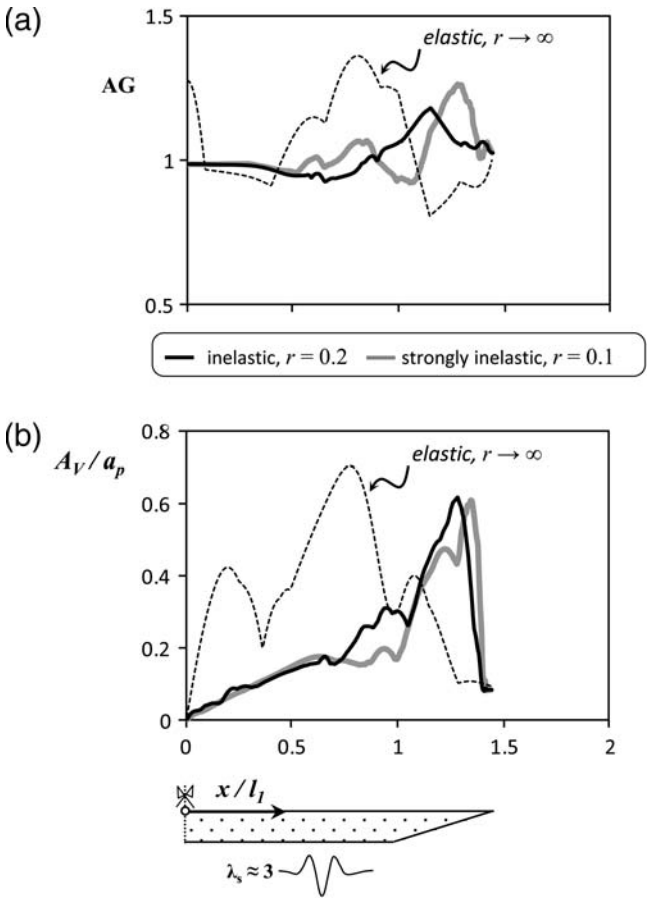

Figure 17. The effect of resistance ratio r on the spatial distribution of (a) aggravation factor AG and (b) dimensionless maximum vertical acceleration A_V/a_p along the valley surface.

$tan\theta = 0.3$, $r = 0.1$, and $v = 415$ subjected to $\lambda_S = 3$ seismic excitation. Three different impedance ratios are analyzed: a rather high $i \approx 12$, a moderate $i \approx 5$, and a quite low $i \approx 2.5$.

When soil nonlinearity is not taken into account (Fig. 16a), the effect of the impedance contrast is quite predictable: the aggravation AG increases with i. Observe that although the spatial distribution of AG exhibits an obvious similarity among all three cases examined, the actual amplitude of the produced aggravation is indeed quite dependent on the impedance contrast, while for $i = 2.5$ the aggravation is barely noticeable (AG does not exceed a mere 1.05). Moving to higher impedance ratios, AG increases to 1.4 (for $i = 5$) and ultimately to 1.6 for $i = 12$.

Similar trends are observed in terms of A_V/a_p. Quite interestingly, however, even for low impedance ratios where aggravation of the horizontal component is negligible, the geometry-induced parasitic vertical component obtains remarkably high values, reaching 70% or more of the horizontal input acceleration. While the peak value of A_V/a_p is practically insensitive to the impedance ratio i, its distribution along the valley surface is substantially affected, while for $i = 2.5$ the peak A_V/a_p observed close to the valley edges reduces substantially toward the valley center. For $i = 12$, a noticeably broader area suffers from large vertical acceleration A_V/a_p. In this latter case, the abrupt fluctuations of A_V/a_p and the multiple peaks at roughly 0.7 may be seen as the signature of the high impedance contrast.

Quite notably, when soil nonlinearity is accounted for (Fig. 16b), all aforementioned phenomena tend to become much less pronounced. Soil plastification dominates the response, drastically overshadowing any effect of the impedance contrast. As a result, the response proves to be remarkably similar in all cases examined both in terms of amplitude and distribution of AG, which hardly differs from one and A_V/a_p.

The Effect of Resistance Ratio r

As stated previously, the resistance ratio r can be considered to be an index of the mobilization of the soil shear strength by the earthquake. The way it has been defined (see equation 12), low values of the resistance ratio r are associated with strongly inelastic behavior. In order to illustratively demonstrate the influence of the resistance ratio on 2D valley response, a valley of $i = 5$, $s = 10.83$, $\tan\theta = 0.3$, and $v = 415$ is subjected to $\lambda_S = 3$ seismic excitation (i.e., relatively long wavelength) varying only the resistance ratio r from 0.2 (nonlinear response) to 0.1 (strongly nonlinear response).

Figure 17 displays the comparison in terms of distribution of AG and A_V/a_p along the valley surface (the dotted line refers to viscoelastic soil response, or equivalently $r \to \infty$). Corroborating the mechanisms highlighted in the preceding sections, it is observed that as the induced nonlinearity increases, 2D effects become more and more concentrated close to the valley edges, and the aggravation AG tends to diminish toward the valley center (Fig. 17a). The differences are proportional to the magnitude of the developing shear strains: under strongly nonlinear response ($r = 0.1$), the stresses applied by the earthquake result in larger shear straining of the soil and therefore a lower effective shear modulus G (see e.g., Vucetic and Dobry, 1991, G-γcurves). This decrease in the effective G compared to its small strain value G_o is responsible for the generation of lower wavelengths because the wavelength is proportional to G, which in turn may be trapped within the valley wedges producing the observed amplification due to their multiple reflections. On the other hand, when the nonlinearity is not that intense ($r = 0.2$), the shear straining of the soil is lower leading to a larger effective G (i.e., closer to G_o). Hence, the produced wavelengths are not as low, and the very convex edge of the valley is not that perceptible. As a result, wave reflections are only possible within a more distant zone where, as explained previously, the density of incoming waves is limited and therefore the produced aggravation is comparatively inferior. In addition to such stiffness effects, the increased effective damping in the system leads to a rigid dissipation

Table 3
Summary of Results on the Effect of Each Dimensionless Factor for the Cases Examined

Dimensionless Factors	AG_{max}	AG_{min}	A_V/a_p
Effect of shape factor s ($\lambda_S = 1$, $i = 5$, $\tan\theta = 0.3$, $v = 415$)			
Elastic Soil Response			
$s = 8.50$	1.20	0.35	1.30
$s = 10.83$	1.07	0.80	1.45
$s = 14.61$	1.35	0.90	1.75
Effect of shape factor s ($\lambda_S = 3$, $i = 5$, $\tan\theta = 0.3$, $v = 415$)			
Elastic Soil Response			
$s = 8.50$	1.40	0.70	0.75
$s = 10.83$	1.40	0.80	0.70
$s = 14.61$	1.30	0.95	0.70
Inelastic Soil Response			
$s = 8.5$	1.35	~1.0	1
$s = 10.83$	1.2	~1.0	0.5
$s = 14.61$	1.2	0.85	0.3
Effect of wavelength ratio λ_S ($i = 5$, $s = 10.83$, $\tan\theta = 0.3$, $v = 415$)			
$\lambda_S = 1$	1.10	0.80	1.50
$\lambda_S = 2$	1.30	0.80	0.70
$\lambda_S = 3$	1.35	0.75	0.70
$\lambda_S = 1$	1.25	0.65	0.85
$\lambda_S = 2$	1.25	0.90	0.60
$\lambda_S = 3$	1.25	0.95	0.40
Effect of impedance ratio i ($s = 10.83$, $\tan\theta = 0.3$, $v = 415$, $\lambda_S = 3$)			
Elastic Soil Response			
$i = 2.5$	1.0	1.0	0.8
$i = 5.0$	1.3	~1.0	0.7
$i = 12.0$	1.6	0.65	0.8
Inelastic Soil Response			
$i = 2.5$	1.25	~1.0	0.5
$i = 5$	1.25	~1.0	0.6
$i = 12$	1.25	0.9	0.6
Effect of resistance ratio r ($i = 5$, $s = 10.83$, $\tan\theta = 0.3$, $v = 415$, $\lambda_S = 3$)			
$\to \infty$ (elastic)	1.40	0.8	0.7
$r = 0.2$	1.15	~1.0	0.6
$r = 0.1$	1.25	0.9	0.6

of Rayleigh waves, and hence at the center of the valleys only vertical *SV* waves may be perceived.

In terms of dimensionless vertical acceleration A_V/a_p (Fig. 17b), the discrepancies are obvious when moving away from the wedge and toward the center of the valley, where the reduction of the vertical component is moderately enhanced with the decrease of r (i.e., for a strongly nonlinear response).

The prevailing role of the mobilization of soil nonlinearity (expressed through the resistance ratio r) becomes evident when recalling the previous discussion of Figures 6 and 7. The example case corresponding to Figure 6 refers to a valley with $i = 5.75$, $\lambda_S = 0.97$, and $r = 0.13$, while that of Figure 7 has $i = 2.88$, $\lambda_S = 5.95$, and $r = 0.39$. Thus, their comparison serves as a perfect example of the cross-effect of these three dimensional ratios. Observe that a strongly inelastic response such as this of Figure 6 is responsible for the creation of a notable shadow zone further enhanced by its considerably low λ_S value. On the other hand, when the induced inelasticity is comparatively lower (Fig. 7) and the λ_S ratio is admittedly high, not only is the shadow zone negligible, but amplification is evident along a significant portion of the valley wedge.

Conclusions

This paper has utilized a specific example to underscore the sensitivity of the response of alluvial valleys to soil inelasticity, thus introducing the necessity of a formal dimensional analysis. The latter was conducted accounting for a fully inelastic soil response facilitating the production of dimensionless results. To this end, this paper has parametrically examined the response of trapezoidal valleys of various geometric and material characteristics (all inspired

by well-documented existing formations) to vertically propagating plane *SV* waves, highlighting the determinative role of a number of dimensionless factors. Collective results are presented in tabular format in Table 3. The key conclusions can be summarized as follows:

(1) As the valley slope becomes gentler, the aggravation AG is more clearly manifested because the generation of numerous reflections within the wedge is more probable, and subsequently the possibility of wave interferences on the surface is enhanced. Conversely, a steep valley boundary may even generate deamplification of the horizontal ground motion. The effect of inclination is drastically limited when nonlinear soil behavior is introduced.

(2) The parasitically generated vertical component A_V/a_p is in general geometry dependent, and thus its amplitude increases as the valley inclination becomes steeper. In the latter case, a significant amount of vertical acceleration is detectable along an extended area on the valley surface.

(3) The ratio of generated wavelengths relative to the valley dimensions λ_S controls the spatial distribution pattern of ground motion aggravation. Consequently, for higher λ_S values and considering elastic soil response, most of the 2D aggravation AG is generated by high amplitude Rayleigh waves; as the λ_S ratio decreases, focusing diffraction of rays within the wedges prevail and peak values of AG shift toward the valley edges.

(4) When nonlinear soil behavior is considered, the 2D response follows a common pattern quite independently of the wavelength ratio λ_S: peak values of both AG and A_V/a_p are constrained near the edges of the valley and indeed in locations where the elastic analysis would even predict a deamplification of the ground motion.

(5) The impedance contrast i has been shown to strongly affect the amplitude of the produced aggravation (but not its spatial distribution pattern) when assuming elastic soil response. Soil inelasticity reduces its effects.

(6) Although accounting for soil nonlinearity has been shown to radically overshadow the effect of most of the examined parameters, the ratio of mobilized soil resistance (expressed through the dimensionless resistance ratio) was not proven to be fundamental.

Data and Resources

All the excitation records utilized in this study are cited mathematical pulses. No additional data have been used. The Ohba Valley soil profile data and geometry have been obtained from the published source listed in the references.

Acknowledgments

This work was partially supported by the European Union Seventh Framework research project funded through the Ideas program of the European Research Council (ERC) in support of frontier research under advanced grant contract number ERC-2008-AdG 228254-DARE. 21. F. Gelagoti would like to acknowledge the support of the research grant Support for Post-Doctoral Researchers (PE8-3886) of GSRT. This research project is cofinanced by the E. U. European Social Fund and National Resources.

References

Aki, K., and K. L. Larner (1970). Surface motion of layered medium having an irregular interface due to incident plane *SH* waves, *J. Geophys. Res.* **75,** 933–954, doi 10.1029/JB075i005p00933.

Anastasopoulos, I., F. Gelagoti, R. Kourkoulis, and G. Gazetas (2011). Simplified constitutive model for simulation of cyclic response of shallow foundations: Validation against laboratory tests, *J. Geotech. Geoenviron. Eng.* **137,** 15, doi 10.1061/(ASCE)GT.1943-5606.0000534.

Archuleta, R. J., P. Liu, J. H. Steidl, L. F. Bonilla, D. Lavallée, and F. Heuze (2003). Finite-fault site-specific acceleration time histories that include nonlinear soil response, *Phys. Earth Planet. In.* **137,** 153–181.

Barenblatt, G. I. (1996). *Scaling, Self-Similarity, and Intermediate Asymptotics*, Cambridge Univ. Press, New York.

Bard, P.-Y., and M. Bouchon (1980a). The seismic response of sediment-filled valleys. Part 1. The case of incident *SH* waves, *Bull. Seismol. Soc. Am.* **70,** 1263–1286.

Bard, P. Y., and M. Bouchon (1980b). The seismic response of sediment-filled valleys. Part 2. The case of incident *P* and *SV* waves, *Bull. Seismol. Soc. Am.* **70,** no. 5, 1921–1941.

Bard, P. Y., M. Campillo, F. J. Chávez-García, and F. J. Sánchez-Sesma (1988). The Mexico earthquake of September 19, 1985: A theoretical investigation of large and small amplification effects in the Mexico City Valley, *Earthq. Spectra* **4,** 609–633.

Benz, H. M., and R. B. Smith (1998). Elastic wave propagation and site amplification in the Salt Lake Valley, Utah, from simulated normal faulting earthquakes, *Bull. Seismol. Soc. Am.* **78,** no. 6, 1851–1874.

Bielak, J., J. Xu, and O. Ghattas (1999). Earthquake ground motion and structural response in alluvial valleys, *J. Geotech. Geoenviron. Eng.* **125,** no. 5, 413–423.

Bodin, P., R. Bilham, J. Behr, J. Gomberg, and K. W. Hudnut (1994). Slip triggered on southern California faults by the 1992 Joshua Tree, Landers, and Big Bear earthquakes, *Bull. Seismol. Soc. Am.* **84,** 806–816.

Boore, D. (1970). Love waves in non-uniform wave guides: Finite difference calculation, *J. Geophys. Res.* **75,** 1512–1527.

Borcherdt, R. D., G. Glassmoyer, A. Der Kiureghian, and E. Cranswick (1989). Results and data from seismologic and geologic studies following earthquakes of December 7, 1988 near Spitak, Armenia, S. S. R., *U. S. Geol. Surv. Open-File Rept. 89-163A*, 188 pp.

Chávez-García, F. J., and P. Y. Bard (1989). Effect of random thickness variations on the seismic response of a soft soil layer: Applications to Mexico City, in *Proc. of the 4th International Conference on Soil Dynam. Earthq. Eng.*, Mexico City, October 1989, 247–261.

Chávez-García, F. J., W. R. Stephenson, and M. Rodriguez (1999). Lateral propagation effects observed at Parkway, New Zealand. A case history to compare 1D versus 2D site effects, *Bull. Seismol. Soc. Am.* **89,** no. 3, 718–732.

Cubrinovski, M., and R. A. Green (2010). Geotechnical reconnaissance of the 2010 Darfield (New Zealand) earthquake, Report No. GEER-024, report of the National Science Foundation-Sponsored Geotechnical Extreme Events Reconnaissance (GEER) Team, 180 pp.

Fishman, K. L., and S. Ahmad (1995). Seismic response for alluvial valleys subjected to *SH*, *P* and *SV* waves, *Soil Dynam. Earthq. Eng.* **14,** 249–258, doi 10.1016/0267-7261(94)00049-M.

Frischknecht, C., P. Rosset, and J.-J. Wagner (2005). Toward seismic microzonation—2-D modeling and ambient seismic noise measurements: The case of an embanked, deep alpine valley, *Earthq. Spectra* **21,** no. 3, 635–652, doi 10.1193/1.1941252.

Gazetas, G., K. Fan, T. Tazoh, and K. Shimizu (1993). Seismic response of the pile foundation of Ohba Ohashi bridge, in *Proc. of the 3rd Int. Conf. on Case Histories in Geotechnical Engineering*, 1803–1809.

Gelagoti, F., R. Kourkoulis, I. Anastasopoulos, T. Tazoh, and G. Gazetas (2010). Seismic wave propagation in a very soft alluvial valley: Sensitivity to ground-motion details and soil nonlinearity, and generation of a parasitic vertical component, *Bull. Seismol. Soc. Am.* **100,** 6, 3035–3054, doi 10.1785/0120100002.

Hanks, T. C. (1975). Strong ground motion of San Fernado, California, earthquake ground displacements, *Bull. Seismol. Soc. Am.* **65,** 193–225.

Hanks, T. C., and A. G. Brady (1991). The Loma Prieta earthquake ground motion and damage in Oakland, Treasure Island, and San Francisco, *Bull. Seismol. Soc. Am.* **81,** 2019–2047.

Harmsen, S., and S. Harding (1981). Surface motion over a sedimentary valley for incident plane *P* and *SV* waves, *Bull. Seismol. Soc. Am.* **71,** no. 3, 655–670.

Hartzell, S., D. Carver, R. A. Williams, S. Harmsen, and A. Zerva (2003). Site response, shallow shear-wave velocity, and wave propagation at the San Jose, California, dense seismic array, *Bull. Seismol. Soc. Am.* **93,** no. 1, 443–464, doi 10.1785/0120020080.

Herrera, I. (1964). A perturbation method for elastic wave propagation I. Nonparallel boundaries, *J. Geophys. Res.* **69,** 3845–3851, doi 10.1029/JZ069i018p03845.

Hill, J., H. Benz, M. Murphy, and G. Schuster (1990). Propagation and Resonance of the *SH* waves in the Salt Lake Valley, Utah, *Bull. Seismol. Soc. Am.* **80,** no. 1, 23–42.

Ishibashi, I., and X. Zhang (1993). Unified dynamic shear moduli and damping ratios of sand and clay, *Soils Found.* **33,** no. 1, 182–191.

Jongmans, D., and M. Campillo (1993). The response of the Ubaye Valley (France) for incident *SH* and *SV* waves: Comparison between measurements and modelling, *Bull. Seismol. Soc. Am.* **83,** no. 3, 907–924.

Jongmans, D., K. Pitilakis, D. Demanet, D. Raptakis, J. Riepl, C. Horrent, G. Tsokas, K. Lontzetidis, and P.-Y. Bard (1998). EURO-SEISTEST: Determination of the geological structure of the Volvi basin and validation of the basin response, *Bull. Seismol. Soc. Am.* **88,** no. 2, 473–487.

Kanai, K. (1951). On the group velocity of dispersive surface waves, *Bull. Earthq. Res. Inst. Tokyo Univ.* **29,** 49–60.

Kawase, H. (1996). The cause of the damage belt in Kobe: "The basin-edge effect," constructive interference of the direct *s*-wave with the basin-induced diffracted/rayleigh waves, *Seismol. Res. Lett.* **67,** no. 5, 25–34, doi 10.1785/gssrl.67.5.25.

Kawase, H., and T. Sato (1992). Simulation analysis of strong motions in the Ashigara Valley considering one- and two-dimensional geological structures, *J. Phys. Earth* **40,** 27–56.

Kudo, K., E. Shima, and M. Sakaue (1988). Digital strong motion accelerograph array in Ashigara Valley, in *Proc. of the 9th World Conf. on Earthquake Engineering*, Tokyo, Japan, 2–9 August 1988, 119–124.

Langhaar, H. L. (1951). *Dimensional Analysis and Theory of Models*, Wiley, New York.

Lenti, L., S. Martino, A. Paciello, and G. Scarascia Mugnozza (2009). Evidence of two-dimensional amplification effects in an alluvial valley (Valnerina, Italy) from velocimetric records and numerical models, *Bull. Seismol. Soc. Am.* **99,** 1612–1635, doi 10.1785/0120080219.

Makris, N., and C. J. Black (2004). Dimensional analysis of bilinear oscillators under pulse-type excitations, *J. Eng. Mech. Div. ASCE* **130,** no. 9, 1019–1031, doi 10.1061/(ASCE)0733-9399(2004)130:9(1019).

Marsh, J., T. J Larkin, A. J. Haines, and R. A. Benites (1995). Comparison of linear and nonlinear seismic responses of two-dimensional alluvial basins, *Bull. Seismol. Soc. Am.* **85,** 874–889.

Olsen, K. B., A. Akinci, A. Rovelli, F. Marra, and L. Malagnini (2006). 3D ground-motion estimation in Rome, Italy, *Bull. Seismol. Soc. Am.* **96,** no. 1, 133–146, doi 10.1785/0120030243.

Pavlenko, O. V. (2001). Nonlinear seismic effects in soils: Numerical simulation and study, *Bull. Seismol. Soc. Am.* **91,** no. 2, 381–396, doi 10.1785/0120000047.

Papageorgiou, A. S., and J. Kim (1991). Study of the propagation and amplification of seismic waves in Caracas Valley with reference to the 29 July 1967 earthquake: *SH* waves, *Bull. Seismol. Soc. Am.* **81,** no. 6, 2214–2233.

Pergalani, F., M. Compagnoni, and V. Petrini (2003). Evaluation of site effects in some localities of 'Alta Val Tiberina Umbra' (Italy) by numerical analysis, *Soil Dynam. Earthq. Eng.* **23,** no. 2, 85–105.

Pitarka, A., and K. Irikura (1996). Basin structure effects on long-period strong motions in the San Fernando Valley and the Los Angeles basin from the 1994 Northridge earthquake and an aftershock, *Bull. Seismol. Soc. Am.* **86,** 126–137.

Pitarka, A., K. Irikura, T. Iwata, and H. Sekiguchi (1998). Three-dimensional simulation of the near-fault ground motion for the 1995 Hyogo-Ken Nanbu (Kobe), Japan, earthquake, *Bull. Seismol. Soc. Am.* **88,** 428–440.

Psarropoulos, P. N., G. Gazetas, and T. Tazoh (1999). Seismic response analysis of alluvial valley at bridge site, in *Proc. of the 2nd Int. Conf. on Geotechnical Earthquake Engineering*, Lisbon, Portugal 41–46.

Ricker, N. (1960). The form and laws of propagation of seismic wavelets, *Geophysics* **18,** 40, doi 10.1190/1.1437843.

Rymer, J. M. (2000). Triggered surface slips in the Coachella Valley area associated with the 1992 Joshua Tree and Landers, California, earthquakes, *Bull. Seismol. Soc. Am.* **90,** no. 4, 832–848, doi 10.1785/0119980130.

Sánchez-Sesma, F. J., and F. Luzón (1995). Seismic response of three-dimensional alluvial valleys for incident *P*, *S*, and Rayleigh waves, *Bull. Seismol. Soc. Am.* **85,** no. 1, 269–284.

Sánchez-Sesma, F. J., J. Ramos-Martinez, and M. Campillo (1993). An indirect boundary element method applied to simulate the seismic response of alluvial valleys for incident *P*, *S*, and Rayleigh waves, *Earthq. Eng. Struct. Dynam.* **22,** 279–295, doi 10.1002/eqe.4290220402.

Scrivner, C. W., and D. V. Helmberger (1999). Finite-difference modeling of two aftershocks of the 1994 Northridge, California, earthquake, *Bull. Seismol. Soc. Am.* **89,** 1505–1518.

Tazoh, T., K. Shimizu, and K. Wakahara (1988). Seismic observations and analysis of grouped piles, *Shimizu Tech. Res. Bull.* **7,** 17–32.

Trifunac, M. D. (1973). A note on scattering of plane *SH* waves by a semi-elliptical canyon, *Int. J. Earthq. Eng. Struct. Dyn.* **1,** 267–281.

Trifunac, M. D. (1971). Surface motion of a semi-cylindrical alluvial valley for incident plane *SH* waves, *Bull. Seismol. Soc. Am.* **61,** 1755–1770.

Tsai, N. C. (1969). Influence of local geology on earthquake ground motion, *California Institute of Technology*, Pasadena, California, http://resolver.caltech.edu/CaltechEERL:1969.EERL.1969.002.

Vidale, J. E., and D. V. Helmberger (1988). Elastic finite-difference modeling of the 1971 San Fernado, California earthquake, *Bull. Seismol. Soc. Am.* **78,** 122–141.

Vucetic, M., and R. Dobry (1991). Effect of soil plasticity on cyclic response, *J. Geotech. Geoenviron. Eng.* **117,** no. 1, 89–107, doi 10.1061/(ASCE)0733-9410(1991)117:1(89).

Wong, H. L., and M. D. Trifunac (1974). Surface motion of a semi-elliptical alluvial valley for incident plane *SH* waves, *Bull. Seismol. Soc. Am.* **64,** 1389–1408.

Yegian, M. K., V. G. Ghahraman, and G. Gazetas (1994). Seismological, soil and valley effects in Kirovakan, 1988 Armenia earthquake, *J. Geotech. Geoenviron. Eng.*, **120,** no. 2, 349–365, doi 10.1061/(ASCE)0733-9410(1994)120:2(349).

Zhang, B., and A. S. Papageorgiou (1996). Simulation of the response of the Marina District basin, San Francisco, California, to the 1989 Loma Prieta earthquake, *Bull. Seismol. Soc. Am.* **86,** no. 5, 1382–1400.

School of Civil Engineering
National Technical University of Athens
Zografou-Athens, Greece

Manuscript received 25 June 2011